

# Hippocampal Engrams Generate Variable Behavioral Responses and Brain-Wide Network States

**Kaitlyn E. Dorst,<sup>1,2\*</sup> Ryan A. Senne,<sup>1,2\*</sup> Anh H. Diep,<sup>1</sup> Antje R. de Boer,<sup>1</sup> Rebecca L. Suthard,<sup>1,2</sup> Heloise Leblanc,<sup>1,2</sup> Evan A. Ruesch,<sup>1</sup> Angela Y. Pyo,<sup>1</sup> Sara Skelton,<sup>1</sup> Lucas C. Carstensen,<sup>1,2</sup> Samantha Malmberg,<sup>1,2</sup> Olivia P. McKissick,<sup>1</sup> John H. Bladon,<sup>1</sup> and Steve Ramirez<sup>1</sup>**

<sup>1</sup>Department of Psychological and Brain Sciences, Boston University, Boston 02215, Massachusetts and <sup>2</sup>Graduate Program for Neuroscience, Boston University, Boston 02215, Massachusetts

Freezing is a defensive behavior commonly examined during hippocampal-mediated fear engram reactivation. How these cellular populations engage the brain and modulate freezing across varying environmental demands is unclear. To address this, we optogenetically reactivated a fear engram in the dentate gyrus subregion of the hippocampus across three distinct contexts in male mice. We found that there were differential amounts of light-induced freezing depending on the size of the context in which reactivation occurred: mice demonstrated robust light-induced freezing in the most spatially restricted of the three contexts but not in the largest. We then utilized graph theoretical analyses to identify brain-wide alterations in cFos expression during engram reactivation across the smallest and largest contexts. Our manipulations induced positive interregional cFos correlations that were not observed in control conditions. Additionally, regions spanning putative “fear” and “defense” systems were recruited as hub regions in engram reactivation networks. Lastly, we compared the network generated from engram reactivation in the small context with a natural fear memory retrieval network. Here, we found shared characteristics such as modular composition and hub regions. By identifying and manipulating the circuits supporting memory function, as well as their corresponding brain-wide activity patterns, it is thereby possible to resolve systems-level biological mechanisms mediating memory’s capacity to modulate behavioral states.

**Key words:** engram; fear; hippocampus; learning; memory; networks

## Significance Statement

Implementing appropriate defensive behaviors across disparate environments is essential for survival. Memories can be used to select these responses. Recent work identified and artificially manipulated cellular ensembles (i.e., memory engrams) within the hippocampus that mediate fear memory retrieval, yet how these populations engage brain-wide pathways that mediate defensive behaviors, such as freezing, under different environments remains unclear. We demonstrated here that reactivation across environments of various sizes elicits different freezing responses and corresponding brain-wide network dynamics. These findings establish the flexibility of memory-bearing ensembles in generating brain and behavior states.

Received Feb. 21, 2023; revised Oct. 31, 2023; accepted Nov. 13, 2023.

Author contributions: K.E.D., R.A.S., L.C.C., S.M., and S.R. designed research; K.E.D., R.A.S., A.H.D., A.R.B., R.L.S., H.L., E.A.R., A.Y.P., S.S., L.C.C., S.M., O.P.M., J.H.B. performed research; K.D., R.A.S., J.H.B., and S.R. contributed unpublished reagents/analytic tools; K.E.D., R.A.S., R.L.S. analyzed data; K.E.D., R.A.S., and S.R. wrote the paper.

This work was supported by the Ludwig Family Foundation, an NIH Early Independence Award (DP5 OD023106-01), an NIH Transformative R01 Award, a Young Investigator Grant from the Brain and Behavior Research Foundation, the McKnight Foundation Memory and Cognitive Disorders Award, the Pew Scholars Program in the Biomedical Sciences, the Chan Zuckerberg Foundation, the Air Force Office of Scientific Research (FA9550-21-1-0310), the Neurophotonics Center at Boston University, and the Center for Systems Neuroscience at Boston University.

\*K.E.D. and R.A.S. contributed equally to this work.

The authors declare no competing financial interests.

A.R.B.’s present address: University of Groningen, Groningen 9712 CP, The Netherlands.

E.A.R.’s present address: Brain and Cognitive Sciences Program, Massachusetts Institute of Technology, Cambridge 02139, Massachusetts.

O.P.M.’s present address: The Neuroscience Graduate Program, Brown University, Providence 02912, Rhode Island.

Correspondence should be addressed to Steve Ramirez at dvsteve@bu.edu.

<https://doi.org/10.1523/JNEUROSCI.0340-23.2023>

Copyright © 2024 the authors

## Introduction

All animals utilize a repertoire of defensive strategies to avoid danger under a variety of environmental conditions. For instance, it could be more advantageous to hide when hunted in a densely forested area, yet fleeing could be more advantageous in a vast field. The brain performs a series of computations to integrate important contextual information that dictates appropriate behavioral outputs (Fanselow, 1994; Gross and Canteras, 2012; Silva et al., 2016). The defensive strategies chosen, such as freezing in a forest or fleeing in a field, can be learned and used to guide the animal in future scenarios.

Memory systems play an important role in mediating defensive actions based on past events. This helps the animal avoid potentially harmful scenarios or cope with similar threatening situations. The hippocampus is an evolutionarily conserved region crucial to episodic memory processes that guide defensive

actions during fear memory retrieval, and lesions show that hippocampal disruption can impair such behavioral responses (Scoville and Milner, 1957; Kim et al., 1993; Fanselow, 1994; Maren et al., 2013). Populations of cells within the hippocampus, often termed “engram” ensembles, are both necessary and sufficient to drive memory expression (Liu et al., 2012; Chen et al., 2019; Josselyn and Tonegawa, 2020). Activity-dependent and inducible tagging systems have allowed researchers to artificially manipulate engrams encoding fearful experiences to drive defensive actions (Reijmers et al., 2007). Many of these studies measured freezing behavior when a hippocampal fear engram is reactivated in a novel context (Liu et al., 2012; Ryan et al., 2015; Roy et al., 2016). However, recent reports show that hippocampal fear engrams can drive place aversion or anxiety-related avoidance-like responses instead of freezing (Ramirez et al., 2013; Redondo et al., 2014; Chen et al., 2019). This alludes to the possibility tested here that hippocampal fear engrams are flexible in their capacity to drive state-dependent alterations in behavioral outputs contingent on external demands. How these discrete populations can engage underlying neural systems to gate defensive behaviors is relatively unknown.

To gain mechanistic insight into memory-driven defensive behaviors, we leveraged activity-dependent, inducible tagging strategies to optogenetically manipulate hippocampal fear engrams in freely behaving mice. We first tagged a hippocampal fear engram in the dentate gyrus (DG) subregion with channelrhodopsin-2 (ChR2) during contextual fear conditioning (CFC). Over subsequent days, mice were then subjected to optogenetic reactivation in a set of different sized environments. Our findings show that the tagged hippocampal CFC engram is not fixed to a singular defensive response during optogenetic reactivation, as mice engaged in freezing when the hippocampal fear engram was reactivated in a small arena but not in a large area.

Moreover, a variety of neural circuits are implicated in mediating defensive actions. These areas span putative “fear” and “defense” systems for sensory detection, integration, and commanding behavior output (Fendt and Fanselow, 1999; Gross and Canteras, 2012; Tovote et al., 2015; Silva et al., 2016). Recent technological advancements in whole-brain clearing, immunolabeling, and light-sheet microscopy allow researchers to take an unbiased approach to examine interactions between these systems with mesoscale resolution (Dean et al., 2015; Kim et al., 2015; Park et al., 2019; Swaney et al., 2019; Yun et al., 2019). Using these approaches, we examined brain-wide pairwise correlations of endogenous cFos expression in mice that underwent optogenetic reactivation of the hippocampal CFC engram in either the smallest arena or the largest, as those environments promoted and discouraged light-induced freezing, respectively. We then utilized network analyses to examine the topological nature of the functional interactions between brain areas and then identified mediator “hub” regions that were crucial to the resulting graphs. We found that hippocampal CFC engram reactivation greatly increased brain-wide cFos correlation. The respective functional networks differed in their topological structure—suggesting that each condition produced unique brain states. Regions in fear and memory systems were differentially recruited as hub regions across experimental conditions.

Together, our results show that hippocampal CFC engrams drive behavioral outputs that are contingent on environmental parameters such as size. These outputs uniquely engage brain-wide processes and point to numerous hub regions as sites for

future perturbation studies. The flexibility of hippocampal CFC engrams underscores the dynamic nature of memory-guided behavior and offers a new dimension to intervening with disorders of the brain in which fear is a core component, such as post-traumatic stress disorder and anxiety.

## Methods

### Animals

Wild-type males (2–3 months of age; Charles River Laboratories) were housed in groups of 3–4 per cage. Aggressor mice were separated from cagemates as needed and were single housed with extra enrichment. All mice were kept on 12:12 light/dark cycles (0700–1900) in humidity-controlled colony rooms and had *ad libitum* access to standard rodent chow and water. Upon arrival at the facility, mice were left undisturbed for 3 d. We substituted the rodent chow with 40 mg/kg doxycycline (DOX) chow 24 h prior to surgery. Surgerized mice were left undisturbed for 10 d to recover. All subjects were treated in accordance with protocol 201800579 approved by Boston University’s Institutional Animal Care and Use Committee (IACUC Protocol 17-008).

### Viruses

The two viruses for the activity-dependent tagging system were packaged at the University of Massachusetts Amherst Viral Vector Core. The first virus contains a pAAV-cFos-tTA plasmid vector and the second a pAAV-TRE-ChR2-eYFP (or TRE-eYFP for control experiments). Neural activity induces the expression of the AAV9-cFos-tTA construct and generates tTA proteins in cells. The tetracycline transactivator (tTA) proteins then bind to the tetracycline response element (TRE) to induce the expression of either -ChR2-eYFP or -eYFP. This system is regulated by DOX, a tetracycline derivative, for strict temporal control over when cells are labeled. The removal of DOX from the system opens a tagging window to allow tTA to bind to TRE.

### Surgical procedures

Mice were placed in an induction chamber and anesthetized with a mixture of 4% isoflurane and 70% oxygen and were maintained at 2% isoflurane when mounted in the nosecone of the stereotaxic frame (Kopf Instruments). We applied ophthalmic ointment to both eyeballs to prevent them from drying during surgery. Hair was removed via topical application of hair removal cream, and the scalp was cleaned with ethanol and betadine. We then applied 2% lidocaine (Clipper Distributing Company) to the surface of the scalp for topical analgesia. We made a scalp incision to expose the skull. Peroxide was applied to the surface of the skull to bleach the skull sutures, and the skull was then leveled between bregma and lambda. Bilateral craniotomies were made above the site of the viral injection.

All injection coordinates are in relation to bregma (in mm): for the DG, AP = −2.2, ML = ±1.3, and DV = −2.0. A 33-gauge beveled needle connected to a 10  $\mu$ l Hamilton syringe attached to a micro-infusion pump (UMP3, World Precision Instruments) was used for the viral injections. The needle was lowered 0.2 mm past the injection site and was kept stationary for 2 min. We then raised the needle to the site of injection and waited 1 min before virus infusion. We bilaterally injected the DG with 200 nl of the AAV9-cFos-tTA and AAV9-TRE-ChR2-Venus viral cocktail at a rate of 110 nl/min. Five minutes after the injection was complete, we then moved the needle 0.2 mm above the injection site and waited another 3 min before complete needle removal. DG-injected mice were then implanted with bilateral fiber optics (200  $\mu$ m core diameter; Doric Lenses) directly above the site of viral injection (−1.8 DV). Skull screws were anchored for implant support. We applied layers of metabond and dental cement (A-M Systems) to create a cap over the skull. All mice received a 0.1 ml intraperitoneal injection of 0.3 mg/ml buprenorphine, a subcutaneous 0.5 mg/ml injection of meloxicam, and 0.2 ml of subcutaneous saline following surgery and were placed on a heating pad until conscious recovery.

### Fear conditioning and tagging

All mice were handled for 2 d prior to experiments. After the second day of handling, the DOX diet was swapped with rodent chow, and the animals were left undisturbed for 2 d prior to CFC. This opened the window for activity-dependent viral labeling during the CFC tagging period. Mice were placed in either a standard conditioning chamber with plexiglass walls and a grid floor (17.78 cm L × 17.78 cm W × 30.48 cm H; Coulbourn Instruments) or a custom-built large arena with a series of connected grid floors (57 cm L × 53 cm W × 51 cm H). These grid floors were connected to precision shockers and delivered a series of four foot shocks (2 s, 0.5 mA intensity) throughout the duration of the 8 min tagging session. Mice were placed back on the DOX diet in a clean cage immediately after tagging and remained on DOX for the duration of the experiment. Video data were collected via overhead cameras (Computar) that interface with FreezeFrame (Actimetrics). FreezeFrame can both control the delivery of the foot shocks and perform rudimentary freezing analyses. Freezing during CFC was defined as bouts of 1.25 s or longer with minimal changes in pixel luminance as defined by a numeric pixel threshold,  $N$ .

### Optogenetics

We tested each patch cord before optogenetic experiments to ensure that each patch cord generated at least ~10 mW of power. Fiber-optic implants were plugged into a patch cord connected to a 450 nm laser diode (Doric Lenses). For the large, medium, and small arena sessions, mice were allowed to freely explore for 10 min. Each session began with a 2 min baseline period followed by two duty cycles of optogenetic stimulation. Each duty cycle began with a 2 min light stimulation (light-ON; 20 Hz, 10 ms pulses) followed by 2 min of no light (light-OFF). At the end of the final light-OFF epoch, mice were unplugged from the patch cord and returned to their home cage.

### Behavioral assays

All behavioral assays were conducted during the light cycle (0700–1900). During this time, mice had *ad libitum* access to DOX chow (or regular chow for the natural retrieval group) and water. Any noticeable aggressor mouse was separated to prevent any injury to cagemates.

**Large box.** The large environment was a 63 cm L × 63 cm D × 45.5 cm H arena with opaque walls and a white matte bottom. The center of the chamber was demarcated with a 32 cm × 32 cm square. We additionally introduced an orange scent and dimmed the overhead lighting as new contextual information. Mice were allowed to freely explore for 10 min. Optogenetic stimulation was delivered as described above.

**Medium box.** This experiment was conducted in a conditioning chamber normally suited for rats (30.48 cm L × 25.4 cm W × 30.48 cm H; Coulbourn Instruments). We taped laminated sheets of paper with a cross-hatched design to the walls and placed the laminated paper with a vertical bar pattern on the floor to eliminate any contextual similarities. We additionally introduced a vanilla scent. Mice were allowed to freely explore for 10 min. Optogenetic stimulation was delivered as described above.

**Small box.** This session was performed in a conditioning chamber different from the one that was used for fear conditioning tagging (17.78 cm L × 17.78 cm W × 30.48 cm H; Coulbourn Instruments). We taped laminated sheets with a vertical bar design to the walls of the chamber and placed a solid opaque plastic insert on the bottom of the chamber. We additionally introduced an almond scent in the room. Mice were allowed to freely explore the MB for 10 min. Optogenetic stimulation was delivered as described above.

**Natural retrieval.** Mice dedicated to the natural retrieval group were subjected to CFC as previously described (see Fear conditioning and tagging). However, these mice were not surgerized and therefore did not have any engram tagging. They were placed back in the original chamber in which they received CFC 24 h later for a 3 min period. We define the natural retrieval of a fear memory as occurring within the first 3 min of

context reexposure to prevent any extinction-like phenomena (Sierra-Mercado et al., 2011; Milad and Quirk, 2012). The size of the chamber was similar to that of the small box (SB) condition (17.78 cm L × 17.78 cm W × 30.48 cm H; Coulbourn Instruments) but with no alterations to walls, scent, or flooring.

### Behavioral analysis

Video data from the behavioral assays were taken using GoPro cameras and analyzed using video tracking software (ANY-maze). The total time spent in the center for the large box (LB) sessions and total time freezing for all experimental sessions were automatically quantified and binned into 2 min intervals corresponding to the light epoch. Rearing and self-grooming were manually quantified by experimenters blind to the animal identification. For the natural retrieval group, FreezeFrame software quantified and binned freezing across the 3 min session.

### Immunohistochemistry

All mice were transcardially perfused 90 min after the first bin of optogenetic stimulation with 4°C phosphate-buffered saline (PBS) followed by 4% paraformaldehyde (PFA) in PBS.

All brains for slice immunohistochemistry were stored in PFA for 48 h prior to slicing. Brains were serial sectioned in 50  $\mu$ m increments using a vibratome (Leica, VT100S) and collected in cold PBS. We collected slices containing the DG as needed. All slices were incubated for 2 h at room temperature in a 1× PBS + 0.2% Triton (PBST) and 5% normal goat serum (NGS) on an orbital shaker (Amazon). Slices were then transferred to wells containing a primary antibody solution [1:1,000 rabbit anti-cFos (Synaptic Systems), 1:1,000 chicken anti-GFP (Invitrogen)] and were left to incubate for 48 h on an orbital shaker at 4°C. Slices were washed with PBS for 40 min (20 min 2×) followed by incubation with a secondary antibody solution [1:200 Alexa 555 anti-rabbit (Invitrogen); 1:200 Alexa 488 anti-chicken (Invitrogen)]. After incubation, slices were washed once more as previously described and mounted onto microscope slides (VWR International). Cell nuclei were counterstained with DAPI added to Vectashield HardSet Mounting Medium on a coverslip and were left to dry overnight.

### Confocal microscopy and cell quantification

To confirm virus expression, we acquired images using an LSM-800 confocal microscope with a 20× objective lens (Carl Zeiss AG). Each image of the region of interest (ROI) contained 20 slices in a z-stack with a step size of 1.54  $\mu$ m. We additionally set a series of tiles with a 10% overlap to create a single image of the ROI. Images were captured either manually with no focus strategy or were automated using the software autofocus feature in Zen Blue (ver. 2.3) to detect the most intense fluorescent pixels within the defined z-stack. All DAPI and cFos cells were quantified using a machine learning approach (Berg et al., 2019). Ensemble overlap between endogenous cFos and the tagged hippocampal CFC engram was manually quantified by experimenters blind to the animals' condition. For ChR2 SB overlap statistics (Fig. 6C), we extrapolated the average granule cell density measurement from Keller et al. (2018) to compare our ensemble overlap relative to chance, which we define as:

$$(\# \text{ of GFP+ cells} / (\# \text{ of GFP+ cells} / 7935) * (\# \text{ of cFos+ cells} / 7935))$$

### LifeCanvas Technologies

Brains for network analyses were stored in PFA for 24 h after perfusion and extraction. They were then stored in 0.02% sodium azide solution before being sent to LifeCanvas Technologies for brain-wide cFos detection.

Once there, brains undergo a series of preservation and clearing steps using SHIELD (Park et al., 2019) and SmartClear Pro technology (Kim et al., 2015), respectively. The samples are then washed and prepped for organ-scale immunolabeling using SmartLabel reagents (Yun et al., 2019). Samples are batch labeled in 5  $\mu$ g goat anti-GFP and 3.5  $\mu$ g rabbit anti-cFos per brain using SmartBatch and are left to incubate for roughly 18 h. Then, samples undergo a series of washes and fixation steps over subsequent days before being incubated in secondary solutions (Yun et

al., 2019). Finally, brains are mounted in agarose + EasyIndex solution for image preparation.

Brain-wide images are acquired using a SmartSPIM microscope equipped with a  $3.6\times$  objective with a  $1.8\text{ }\mu\text{m} \times 1.8\text{ }\mu\text{m}$  pixel size and a  $z$ -step size of  $4\text{ }\mu\text{m}$ . The axial resolution of the images is  $<4.0\text{ }\mu\text{m}$ . Tile correcting and destriping are also applied as described in Swaney et al. (2019). The samples are imaged using three channels: 488 nm (autofluorescence/NeuN), 561 nm (GFP), and 642 nm (cFos).

The autofluorescence channel is used to align the images to the Allen Brain Atlas (Allen Institute for Brain Science: <https://portal.brain-map.org/>). LifeCanvas Technologies carries out this alignment process in two phases. The first phase is an automated process that samples 10–20 atlas-aligned reference samples for each brain sample using a variety of SimpleElastix warping algorithms. An average alignment was computed for all other intermediate images. To confirm the efficacy of the alignment algorithm, the second phase uses a custom Neuroglander interface (Nugget: <https://github.com/chunglabmit/nugget>) for manual confirmation of the automated alignment algorithm. The researcher would adjust correspondence points between the atlas and the sample image as needed to ensure more rigid alignment.

Once the images were aligned, cell populations were then mapped onto the atlas for region-specific quantification. LifeCanvas Technologies developed a custom convolutional neural network using the TensorFlow Python package (Google). Cell detection was performed by two networks in sequence. A fully convolutional detection network (Shelhamer et al., 2016) based on a U-Net architecture (Ronneberger et al., 2015) was used to find possible positive locations. Second, a convolutional network using a ResNet architecture (He et al., 2015) was used to classify each location as positive or negative. Once the cells were aligned and quantified, cFos data were aggregated into .csv files and sent back to the Ramirez group for further analyses as described below.

#### Network generation and analysis

Networks and all subsequent analysis thereof were generated using custom Python (ver. 3.9.12) scripts built upon networkx (ver. 2.8.4), scipy (ver. 1.8.0), matplotlib (ver. 3.5.2), numpy (ver. 1.22.0), pandas (ver. 1.4.3), seaborn (ver. 0.11.2), statsmodels (ver. 0.13.2), sklearn (ver. 1.2.1), markov\_clustering (ver. 0.0.06), and the brain connectivity toolbox (ver. 0.6.0). For network creation, we first finalized the number of ROIs from the datasheets obtained from LifeCanvas Technologies.

**Network creation.** To model whole-brain cFos density data as a correlational network, we defined a graph structure such that a graph  $G$  is defined as the tuple of edges and vertices,  $(V, E)$ , where  $V$  is the set of nodes that are in the graph and  $E$  is the connections between nodes that are in  $V$ , or otherwise stated:

$$G = (V, E), V = \{v \mid v \in G\}, E = \{(e_i, e_j) \mid (e_i, e_j) \in V \text{ } e_i \neq e_j\}$$

To generate networks, we discarded any region that was a layer of an ROI (e.g., layer 2/3 of the motor cortex) or an entry that was inclusive of several distinct ROIs (e.g., isocortex). Additionally, we eliminated registered fiber tracts and ventricular systems. The remaining brain regions were now the set  $V$ , of nodes that would be used to create our graphs. After extraneous entry elimination, we averaged hemispheric entries to obtain a bilateral density value for each ROI for each animal. From there, inter-region Spearman correlation values were calculated from these density metrics across all animals in the respective experimental conditions. These Spearman correlation coefficients thus became the edges between nodes, meaning that the correlation coefficients were the weights associated between nodes, meaning that we created an undirected, weighted graph. Restated, the networks were created such that the ROIs were nodes, while the  $R_s$  values between them were our weighted edges. Importantly, only Spearman coefficients that survived a 5% FDR correction for significance were included. Intra-network communities were identified by the Leiden algorithm (Traag et al., 2019). The Leiden

algorithm is an improvement on the popular Louvain algorithm. The Louvain algorithm, while powerful, has been shown to sometimes yield badly connected communities. Furthermore, it is nondeterministic, and thus its results can change entirely on its seed and the iterations used. The Leiden algorithm, however, has been proven to converge on optimally assigned communities and is thus a fully superior algorithm. For our implementation, we used the leiden\_communities() method in igraph (ver. 10.0.4). We used CPM as the objective function and the Spearman correlations for our weights. We did a parameter search over 10,000 values between 0.5 and 1.75 for the resolution parameter. Whichever parameter yielded the highest modularity was selected, and we would then run the Leiden algorithm again for 10,000 iterations. We did this for all graphs in our analysis.

**UMAP.** UMAP is a nonlinear dimensionality reduction technique that seeks to approximate a Riemann manifold that a collection of data sits on (McInnes et al., 2020). To do this analysis, we used the Python umap-learn package (ver. 0.5.3). We found that the default arguments of the package were successful at reasonably separating our data, except for the  $n_{neighbors}$  parameter, which we set to be 12. We colored our plots of the Spearman values in UMAP space both by condition and parent brain region (i.e., cortical plate) to determine how our data were clustering.

#### Network statistics

1. **Degree centrality:** Degree centrality measures the importance of a node in a network based on the number of connections it has. It is defined as the fraction of nodes to which a given node is directly connected. Mathematically, the degree centrality ( $C_d$ ) of a node “ $i$ ” in a network with “ $N$ ” nodes is calculated as:

$$C_d(i) = \frac{(k_i)}{(N - 1)}$$

where  $k_i$  is the number of edges connected to node “ $i$ ” and  $(N-1)$  is the maximum possible degree in the network.

2. **Betweenness:** Betweenness centrality quantifies the extent to which a node lies on the shortest paths between pairs of other nodes in a network. It measures the node's ability to bridge different parts of the network. Mathematically, the betweenness centrality ( $C_b$ ) of a node “ $i$ ” is calculated as the sum of the fraction of shortest paths passing through “ $i$ ” over all pairs of nodes “ $s$ ” and “ $t$ ”:

3.

$$C_b(i) = \sum_{s \neq i \neq t} \frac{\sigma_{st}(i)}{\sigma_{st}}$$

where  $\sigma_{s,t}$  is the total number of shortest paths from node “ $s$ ” to node “ $t$ ” and  $\sigma_{s,t(i)}$  is the number of those paths that pass through node “ $i$ .”

4. **Eigenvector centrality:** Eigenvector centrality assigns a score to each node in a network based on the scores of its neighboring nodes. It takes into account not only the number of connections but also the importance of the nodes it is connected to. Mathematically, the eigenvector centrality ( $C_e$ ) of a node “ $i$ ” is calculated as:

5.

$$C_e(i) = \lambda^{-1} \cdot \sum A_{ij} \cdot C_e(j)$$

where  $A_{ij}$  is the adjacency matrix representing the connections between nodes,  $C_e(j)$  is the eigenvector centrality of node “ $j$ ”, and  $\lambda$  is the largest eigenvalue of the adjacency matrix.

6. **Closeness:** Closeness centrality measures how close a node is to all other nodes in the network. It quantifies the average distance from a node to all other nodes in terms of shortest paths.

Mathematically, the closeness centrality ( $C_c$ ) of a node “ $i$ ” is calculated as the reciprocal of the average shortest path length from “ $i$ ” to all other nodes:

$$C_c(i) = \frac{1}{\frac{1}{N} \sum d(i, j)}$$

where  $d(i, j)$  is the shortest path length between nodes “ $i$ ” and “ $j$ .“

7. Clustering coefficient: The clustering coefficient measures the degree to which nodes in a network tend to cluster together. It captures the level of connectivity between a node’s neighbors. Mathematically, the clustering coefficient ( $C$ ) of a node “ $i$ ” is calculated as the ratio of the number of existing connections between the neighbors of “ $i$ ” to the total possible number of connections between them:

$$C(i) = \frac{(2 \cdot E_i)}{(k_i \cdot (k_i - 1))}$$

where  $E_i$  is the number of edges between the neighbors of node “ $i$ ” and  $k_i$  is the degree of node “ $i$ .“

8. Within-module degree z-score (WMDz): The WMDz measures the extent to which a node’s degree is higher or lower than expected within its own module in a modular network. It quantifies how well-connected a node is within its own community compared to the rest of the network. The WMDz score of a node “ $i$ ” in a module “ $m$ ” is calculated as:

$$\text{WMDz}(i) = \frac{(k_i - k_{m_{avg}})}{\sigma_m}$$

where  $k_i$  is the degree of node “ $i$ ,“  $k_{m_{avg}}$  is the average degree of all nodes in module “ $m$ ,“ and  $\sigma_m$  is the standard deviation of degrees in module “ $m$ .“

9. Participation coefficient (PC): The PC measures the extent to which a node connects to different modules in a network. It quantifies the diversity of a node’s connections across modules. Mathematically, the PC of a node “ $i$ ” is calculated as:

$$PC(i) = 1 - \sum \left( \frac{s_i}{m_i} \right)^2$$

where  $s_i$  is the fraction of links that connect node “ $i$ ” to nodes in module “ $m_i$ “ and  $m_i$  is the fraction of nodes in module “ $m_i$ “ in the entire network.

**Hub identification.** We took two interrelated approaches for identifying putative hubs in our respective networks. The first, which does not rely on how nodes are clustered, examines a series of centrality metrics of individual nodes (van den Heuvel et al., 2010; van den Heuvel and Sporns, 2013; Coelho et al., 2018). These properties include the following: degree (i.e., number of edges connected to a node), betweenness (i.e., how often a node is in the shortest path between all pairs of nodes), closeness (i.e., average length of the shortest possible path between a node and every other node in the graph), eigenvector (i.e., how often a node is connected to highly connected nodes), and clustering coefficient (i.e., how often a node is connected to another node that forms a local clique). We designated a threshold to find nodes that fell in the top 20% of degree, betweenness, closeness, and eigenvector and those that fell in the bottom 20% of the clustering coefficient. Each node that fell in those respective distributions would get a +1 to their “hub score,” and we defined central hubs as nodes having a score of 3 or greater.

The second approach relies on how nodes are functionally segregated after a community detection algorithm is applied. For each node, we calculated the WMDz as a measure of intramodular connectivity (i.e., how many edges connect a node with others in the same module) and PC as a measure of intermodular connectivity (i.e., how many edges connect a node with other nodes in other modules). Modular hubs were considered nodes that had a WMDz score of 1 or greater and a PC score of 0.5 or greater.

### Statistical analysis

The sampling size for each experimental group was determined based on previous studies (Wheeler et al., 2013; Vetere et al., 2017; Roy et al., 2022) to obtain statistical strength in both behavior and network analyses (Terstege and Epp, 2022) and are reported in figure captions. All statistics for behavioral experiments were performed using both Python and GraphPad Prism Version 9.2. Normality tests and respective QQ plots were generated to run appropriate statistical testing. Data were presented in the figures as mean ± SEM. Behavioral data were binned at 2 min intervals that corresponded to light epochs (ON vs OFF), and a repeated-measures two-way analysis of variance (ANOVA) was used to identify differences in behavior across conditions. For datasets with normal distributions, follow-up statistical analyses (i.e., one-way ANOVA, multiple Welch’s  $t$  tests) and *post hoc* analyses (i.e., Tukey’s HSD and Sidak’s) were conducted as appropriate. Nonparametric testing for cell counts (Fig. 1B) was performed using a Mann–Whitney rank test. A one-sample  $t$  test was conducted to compare ensemble overlap compared to chance levels (Fig. 6C). Network statistical analyses were performed using Python 3.9.12. All statistical tests assumed an alpha level of 0.05. Statistical tests are reported in each figure legend with \* $p$ <0.05, \*\* $p$ <0.01, and \*\*\* $p$ <0.001.

## Results

### Environment size constrains light-induced freezing during hippocampal CFC engram reactivation

We tested for the capacity of a hippocampal CFC engram to mediate behavioral changes contingent on external demands placed on the animal, such as environment size. Mice first underwent CFC during a “tagging” phase for activity-dependent labeling of the dedicated engram ensemble with either ChR2-eYFP or eYFP (i.e., control; Fig. 1A,B). We first subjected groups of mice to tagging in a commercially available operant chamber outfitted for mice (Fig. 1A, “small”; see Methods). Over subsequent days, these mice underwent optogenetic reactivation of the tagged hippocampal CFC engram while exploring environments of various sizes (i.e., “Small Box” [SB], “Medium Box” [MB], “Large Box” [LB]). These chambers were contextually distinct from the original fear conditioning chamber to prevent generalization (see Methods).

We first quantified freezing behavior, which is defined as the cessation of all movement with the exception of breathing (Groves and Kelley, 1972), as this is a common rodent behavioral metric of a negative affective state such as fear. Strikingly, we observed that optogenetic reactivation of a hippocampal CFC engram tagged in the small chamber was sufficient to induce freezing in the SB in ChR2-injected animals, whereas in the same animals light-dependent freezing behavior was not observed in the LB (RM one-way ANOVA with a Geisser-Greenhouse correction and Tukey’s multiple comparisons;  $F_{(1.929,15.43)} = 8.239$ ,  $p = 0.0039$ ; LB vs MB,  $p = 0.2700$ ; LB vs SB,  $p = 0.0148$ ; MB vs SB,  $p = 0.0758$ ; Fig. 1C, inset). Although there is no interaction, there was significant variance between the reactivation environment and the light epoch (RM two-way ANOVA with a Geisser–Greenhouse correction; interaction,  $F_{(2.339,18.71)} = 1.977$ ,  $p = 0.1615$ ; environment,  $F_{(1.952,15.61)} = 10.88$ ,  $p = 0.0012$ ; light,  $F_{(1.172,9.38)} = 9.155$ ,  $p = 0.0116$ ; Fig. 1C). We found that there was no difference in freezing behavior in ChR2-injected animals during the initial 2 min baseline period across all three reactivation environments (Tukey’s multiple comparisons; SB vs MB,  $p = 0.9999$ ; MB vs LB,  $p = 0.6863$ ; SB vs LB = 0.1875). Importantly, this relationship between reactivation environment and light-induced freezing is not seen in control animals (Fig. 1D). For the SB condition, there was a significant source of variation from the light term and an interaction between virus condition and light (RM two-way ANOVA with a Geisser–

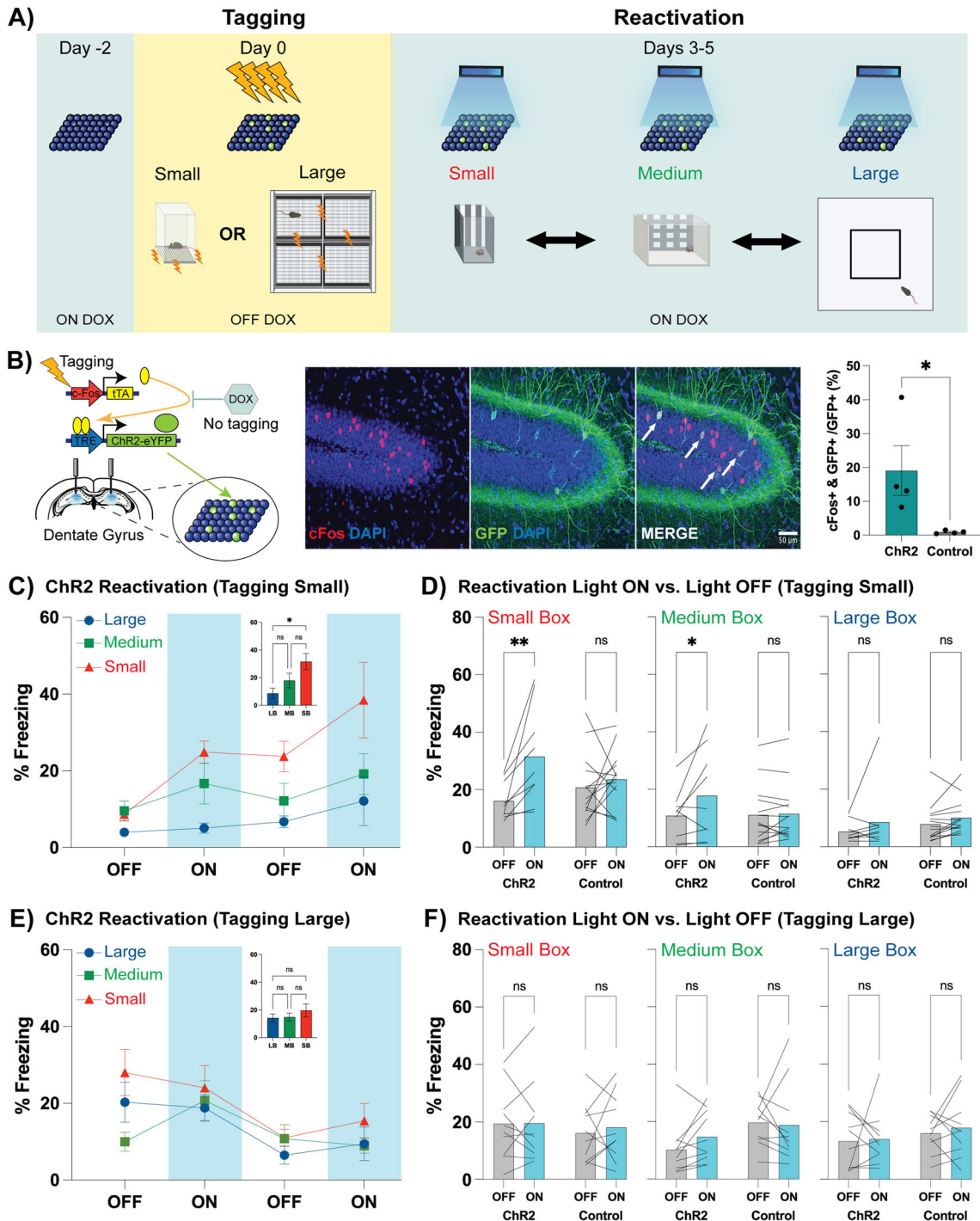


**Figure 1.** Light-induced freezing is contingent on both tagging and reactivation environments. **A**, Behavioral schedule for activity-dependent tagging of a hippocampal CFC engram and reactivation across environments. Mice are taken off of DOX 2 d prior to hippocampal CFC engram tagging. During the CFC session, mice are able to freely explore the environment (small or large chamber) for a handful of minutes before shocks are delivered (4 shocks, 0.5 mA, 2 s). Mice are placed back on the DOX diet after CFC. The tagged hippocampal CFC engram is optogenetically reactivated across 3 d while the mice are exploring novel environments of different sizes (SB, MB, LB). **B**, Schematic representation of the activity-dependent tagging of engram ensembles in the DG (left). Representative 20 $\times$  image of the tagged-GFP + CFC engram (green), endogenous cFos (red), and ensemble overlap (merge, arrows) from a ChR2 animal conditioned in the large chamber (middle). The total number of GFP + and cFos + overlapping cells was divided by the total number of GFP + cells to calculate a reactivation profile (right). There was significantly greater engram reactivation in ChR2 animals when compared to controls. The scale bar represents 50  $\mu$ m. **C**, % Freezing levels for all ChR2 animals conditioned in the small chamber ( $n = 9$ ) binned across 2 min epochs during CFC engram reactivation sessions across all three environments. There was a significant increase in the amount of light-induced freezing in the SB compared to the LB (inset). **D**, Average % freezing across light epochs were compared within ChR2 ( $n = 9$ ) and control ( $n = 14$ ) animals that were conditioned in the small chamber across reactivation environments. The greatest difference in light-induced freezing was observed in ChR2 animals in the SB condition. Additionally, there was a significant difference in light-induced freezing in ChR2 animals in the MB, but no significant light-induced freezing in the LB. There was no significant difference in freezing across epochs in control animals during all three reactivation days. **E**, % Freezing levels for all ChR2 animals conditioned in the large chamber ( $n = 10$ ) binned across 2 min epochs during CFC engram reactivation sessions across all three environments. There was no difference in light-induced freezing in any reactivation environment (inset). **F**, Average % freezing across light epochs were compared within ChR2 ( $n = 10$ ) and control ( $n = 10$ ) animals that were conditioned in the large chamber across reactivation environments. There was no significant difference in freezing across epochs and environments in any group. Data are presented as mean  $\pm$  SEM. Significant differences are reported as \*\* $p$  < 0.01 and \* $p$  < 0.05.

Greenhouse correction; interaction,  $F_{(1,21)} = 4.777, p = 0.0403$ ; virus condition,  $F_{(1,21)} = 0.1625, p = 0.6910$ ; light,  $F_{(1,21)} = 9.852, p = 0.0050$ ). Post hoc mean row comparisons found a significant increase in % freezing during the presentation of light in only ChR2 animals (Sidak's multiple comparisons; ChR2 OFF vs ON,  $p = 0.0052$ ; control OFF vs ON,  $p = 0.7026$ ). For the MB condition, there was also significant variation from the light term and an interaction between light and virus condition (RM two-way ANOVA with a Geisser-Greenhouse correction; interaction,  $F_{(1,21)} = 4.667, p = 0.0424$ ; virus condition,  $F_{(1,21)} = 0.4549, p = 0.5074$ ; light,  $F_{(1,21)} = 5.975, p = 0.0234$ ). Post hoc mean row comparisons also found a significant increase in % freezing during the presentation of light in only ChR2 animals (Sidak's multiple comparisons; ChR2 OFF vs ON,  $p = 0.0152$ ; control OFF vs ON,  $p = 0.9686$ ). For the LB condition, there was no variation from any term or an interaction (RM two-way ANOVA with a Geisser-Greenhouse correction; interaction,  $F_{(1,21)} = 0.1458, p = 0.7064$ ; virus condition,  $F_{(1,21)} = 0.6075, p = 0.4444$ ; light,  $F_{(1,21)} = 3.819, p = 0.0641$ ). Additionally, there were no differences across light epochs with post hoc mean row comparisons (Sidak's multiple comparisons; ChR2 OFF vs ON,  $p = 0.2763$ ; control OFF vs ON,  $p = 0.3957$ ).

We speculated that the observed context-dependent, light-induced freezing in the SB during reactivation was caused by a similar spatial representation of the original small CFC chamber. This has gained further credence in recent findings that demonstrated contextual congruence between encoding and retrieval to promote state-dependent freezing behavior (Meyer et al., 2017; Jung et al., 2023). To test this idea, we constructed a new CFC chamber with similar dimensions to our LB arena to determine if an engram tagged during CFC in a spatially large chamber has the ability to drive context-dependent freezing behavior during reactivation across environmental conditions (Fig. 1A, “large”; see Methods). Surprisingly, there was only variation from the light term on freezing behavior in ChR2-injected animals during hippocampal CFC engram reactivation across reactivation environments (RM two-way ANOVA with a Geisser-Greenhouse correction; interaction,  $F_{(3,170,28,53)} = 1.641, p = 0.2001$ ; environment,  $F_{(1,367,12,30)} = 1.908, p = 0.1932$ ; light,  $F_{(1,811,16,30)} = 8.474, p = 0.0036$ ; Fig. 1E). There was also no discernible difference when comparing % freezing across light epochs and virus condition (RM two-way ANOVA with a Geisser-Greenhouse correction and Tukey's multiple comparisons; SB: interaction,  $F_{(1,18)} = 0.1223, p = 0.7306$ ; virus condition,  $F_{(1,18)} = 0.2316, p = 0.6362$ ; light,  $F_{(1,18)} = 0.2025, p = 0.6581$ ; ChR2 OFF vs ON,  $p = 0.9969$ ; control OFF vs ON,  $p = 0.8225$ ; MB: interaction,  $F_{(1,18)} = 1.214, p = 0.2851$ ; virus condition:  $F_{(1,18)} = 3.069, p = 0.0968$ ; light,  $F_{(1,18)} = 0.5560, p = 0.4655$ ; ChR2 OFF vs ON,  $p = 0.3726$ ; control OFF vs ON,  $p = 0.9616$ ; LB: interaction,  $F_{(1,18)} = 0.0532, p = 0.8202$ ; virus condition,  $F_{(1,18)} = 1.106, p = 0.3069$ ; light,  $F_{(1,18)} = 0.2537, p = 0.6206$ ; ChR2 OFF vs ON,  $p = 0.9772$ ; control OFF vs ON,  $p = 0.8478$ ; Fig. 1F). Importantly, we found significant overlapping populations of the tagged hippocampal CFC engram and endogenous cFos in the ChR2-injected animals (Mann–Whitney  $U$  test;  $p = 0.0286$ ; Fig. 1B), which suggests that congruent representations within HPC cell populations may not manifest as freezing-related behavior. All groups conditioned in both the small and large chamber differentially increased their freezing behavior during the CFC engram tagging session (Fig. 2). A three-way ANOVA revealed a significant interaction between the time and environment terms as well as the time and virus condition terms, but not across all three terms. There was also a trending effect from the

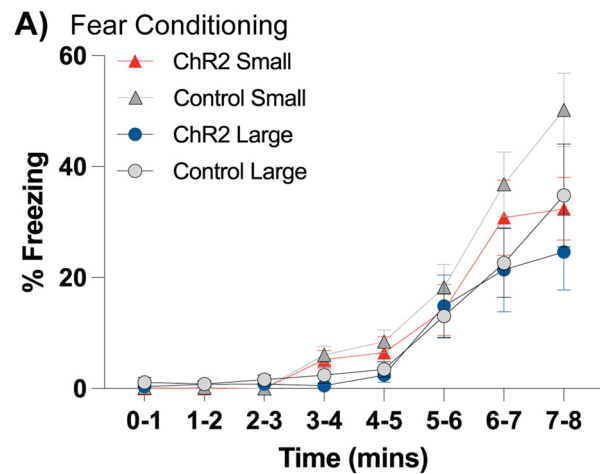


**Figure 2.** CFC in either small or large environments increases freezing behavior. **A**, Average % freezing across time during CFC for ChR2 mice conditioned in the small chamber ( $n = 9$ ; red triangle), Control mice conditioned in the small chamber ( $n = 14$ ; dark gray triangle), ChR2 mice conditioned in the large chamber ( $n = 10$ ; blue circle), and control mice conditioned in the large chamber ( $n = 10$ ; light gray circle). Data are presented as mean  $\pm$  SEM.

environment term and a significant effect of time (RM three-way ANOVA with a Geisser–Greenhouse correction; time  $\times$  environment  $\times$  virus condition,  $F_{(7,273)} = 0.1893, p = 0.9875$ ; environment  $\times$  virus condition,  $F_{(1,39)} = 0.1396, p = 0.7108$ ; time  $\times$  virus condition,  $F_{(7,273)} = 2.158, p = 0.0381$ ; time  $\times$  environment,  $F_{(7,273)} = 2.815, p = 0.0076$ ; virus condition,  $F_{(1,39)} = 1.972, p = 0.1681$ ; environment,  $F_{(1,39)} = 4.077, p = 0.0504$ ; time,  $F_{(2,040,79,55)} = 64.72, p < 0.0001$ ), which points to an intriguing possibility that the environment in which learning occurs can shape behavior during fear memory acquisition.

Since the LB has dimensions commonly associated with open-field assessments for anxiety, we aimed to determine if there were alterations in locomotive patterns such as avoidance of the center of the chamber as well as distance traveled in the LB. We did not observe any differences in avoidance of the center during hippocampal CFC engram reactivation in the LB. Although there was a trending decrease in the % time in center in ChR2 animals conditioned in the small chamber, and a trending effect from the light term, there was no significant difference across the virus condition or an interaction between the virus condition and light terms (RM two-way ANOVA with a Geisser–Greenhouse correction and Sidak's multiple comparisons; interaction,  $F_{(1,21)} = 1.991, p = 0.1729$ ; virus condition,  $F_{(1,21)} = 0.3386, p = 0.5669$ ; light,  $F_{(1,21)} = 3.496, p = 0.0755$ ; ChR2 OFF vs ON,  $p = 0.0932$ ; control OFF vs ON,  $p = 0.9202$ ; Fig. 3A). For animals conditioned in the large chamber, there was a trending decrease in the % time in center in control animals and a trending effect from the light term, and there was no significant difference across virus condition and light or an interaction between the two terms (RM two-way ANOVA with a Geisser–Greenhouse correction and Sidak's multiple comparisons; interaction,  $F_{(1,18)} = 1.277, p = 0.2733$ ; virus condition,  $F_{(1,18)} = 0.04655, p = 0.8316$ ; light,  $F_{(1,18)} = 3.352, p = 0.0837$ ; ChR2 OFF vs ON,  $p = 0.8603$ ; control OFF vs ON,  $p = 0.0989$ ; Fig. 3B). When examining the distance traveled for animals conditioned in the small chamber, there was a significant effect from the light term; however, post hoc comparisons did not yield any significant difference between the virus condition or an interaction between the two (RM two-way ANOVA with a Geisser–Greenhouse correction and Sidak's multiple comparisons; interaction,  $F_{(1,21)} = 0.1606, p = 0.6926$ ; virus

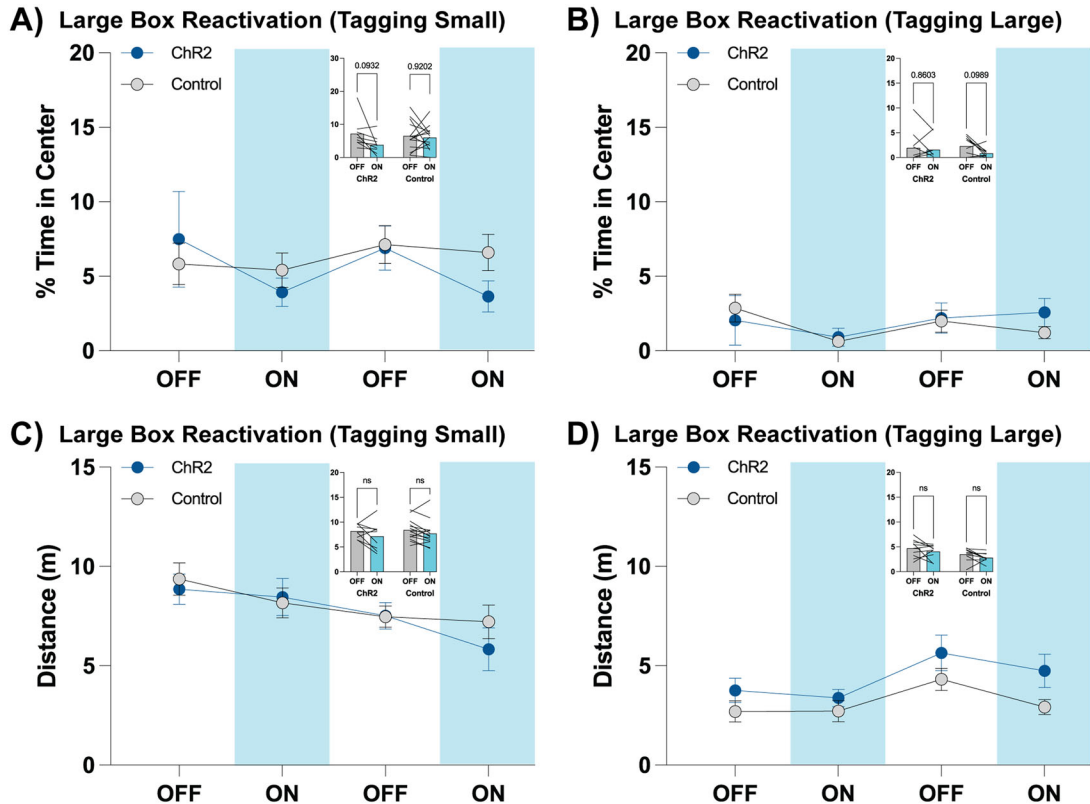


**Figure 3.** Active behaviors such as avoidance and distance are not affected by hippocampal CFC engram reactivation in the LB. **A**, % Time in center of the LB binned across 2 min epochs during CFC engram reactivation in ChR2 animals conditioned in the small chamber ( $n = 9$ ) and control animals conditioned in the small chamber ( $n = 14$ ). % Time in the center of the LB was further averaged across light epochs in the inset. There was a trending, but nonsignificant, decrease in the % time in center during light-ON in the ChR2 animals (inset). **B**, % Time in center of the LB binned across 2 min epochs during CFC engram reactivation in ChR2 animals conditioned in the large chamber ( $n = 10$ ) and control animals conditioned in the large chamber ( $n = 10$ ). % Time in the center of the LB was further averaged across light epochs in the inset. There was a trending, but nonsignificant decrease in the % time in center during light-ON in the control animals (inset). **C**, Distance traveled in the LB binned across 2 min epochs during CFC engram reactivation in ChR2 animals conditioned in the small chamber ( $n = 9$ ) and control animals conditioned in the small chamber ( $n = 14$ ). Distance traveled in the LB was further averaged across light epochs in the inset. There was no difference in distance traveled across all groups and light epochs (inset). **D**, Distance traveled in the LB binned across 2 min epochs during CFC engram reactivation in ChR2 animals conditioned in the large chamber ( $n = 10$ ) and control animals conditioned in the large chamber ( $n = 10$ ). The distance traveled in the LB was further averaged across light epochs in the inset. There was no difference in distance traveled across all groups and light epochs (inset). Data are presented as mean  $\pm$  SEM.

condition,  $F_{1,21} = 0.1898$ ,  $p = 0.6675$ ; light,  $F_{1,21} = 5.201$ ,  $p = 0.0331$ ; ChR2 OFF vs ON,  $p = 0.1908$ ; control OFF vs ON,  $p = 0.2738$ ; Fig. 3C). For animals conditioned in the large chamber, there was significant variation from the virus condition, and a trending effect from the light term, but no interaction between the two terms (RM two-way ANOVA with a Geisser–Greenhouse correction and Sidak's multiple comparisons; interaction,  $F_{1,18} = 0.003848$ ,  $p = 0.9512$ ; virus condition,  $F_{1,18} = 6.007$ ,  $p = 0.0247$ ; light,  $F_{1,18} = 3.248$ ,  $p = 0.0883$ ; ChR2 OFF vs ON,  $p = 0.4138$ ; control OFF vs ON,  $p = 0.3663$ ). Although we found no discernible behavioral phenotypes in the two metrics examined here, we cannot discount additional locomotive patterns that could be modulated by hippocampal CFC engram reactivation.

As there was a lack of observational light-induced freezing behavior in ChR2-injected animals that were conditioned in the large chamber, we sought to quantify nonfreezing behaviors such as rearing and self-grooming, both of which could serve as escape-seeking and stress-coping, respectively (Griebel et al., 1996; Cursio, 2001; Lever et al., 2006; Kalueff et al., 2016; Mu et al., 2020; Liu et al., 2021). In ChR2 animals conditioned in the small chamber, there was no observable light-induced rearing across reactivation environments, yet a significant interaction between the reactivation environment and light variables (RM two-way ANOVA with a Geisser–Greenhouse correction; interaction,

$F_{(2,952,23,62)} = 3.818$ ,  $p = 0.0235$ ; environment,  $F_{(1,275,10,20)} = 0.007015$ ,  $p = 0.9655$ ; light,  $F_{(1,352,10,82)} = 2.659$ ,  $p = 0.1261$ ; Fig. 4A). The two light-ON epochs were further averaged together, but there was no significant difference rearing during reactivation periods across environments (RM one-way ANOVA with a Geisser–Greenhouse correction and Tukey's multiple comparisons;  $F_{(1,394,11,15)} = 0.2854$ ,  $p = 0.6791$ ; LB vs MB,  $p = 0.9651$ ; LB vs SB,  $p = 0.5865$ ; MB vs SB,  $p = 0.8851$ ; Fig. 4A, inset). When compared with control animals, there was no significant difference in % rearing across the virus condition or the light in the SB (RM two-way ANOVA with a Geisser–Greenhouse correction and Sidak's multiple comparisons; interaction,  $F_{(1,21)} = 0.006960$ ,  $p = 0.9343$ ; virus condition,  $F_{(1,21)} = 0.2241$ ,  $p = 0.6408$ ; light,  $F_{(1,21)} = 1.129$ ,  $p = 0.3001$ ; ChR2 OFF vs ON,  $p = 0.7858$ ; control OFF vs ON,  $p = 0.6033$ ), and there was a significant increase in % rearing in control animals during light-ON in the MB (RM two-way ANOVA with a Geisser–Greenhouse correction and Sidak's multiple comparisons; interaction,  $F_{(1,21)} = 0.5588$ ,  $p = 0.4631$ ; virus condition,  $F_{(1,21)} = 0.4023$ ,  $p = 0.5328$ ; light,  $F_{(1,21)} = 15.70$ ,  $p = 0.0007$ ; ChR2 OFF vs ON,  $p = 0.1013$ ; control OFF vs ON,  $p = 0.0023$ ), and there was a significant increase in % rearing in ChR2 animals during light-ON and a trending, but not significant, increase in % rearing in control animals in the LB (RM two-way ANOVA with a Geisser–Greenhouse correction and Sidak's multiple comparisons;

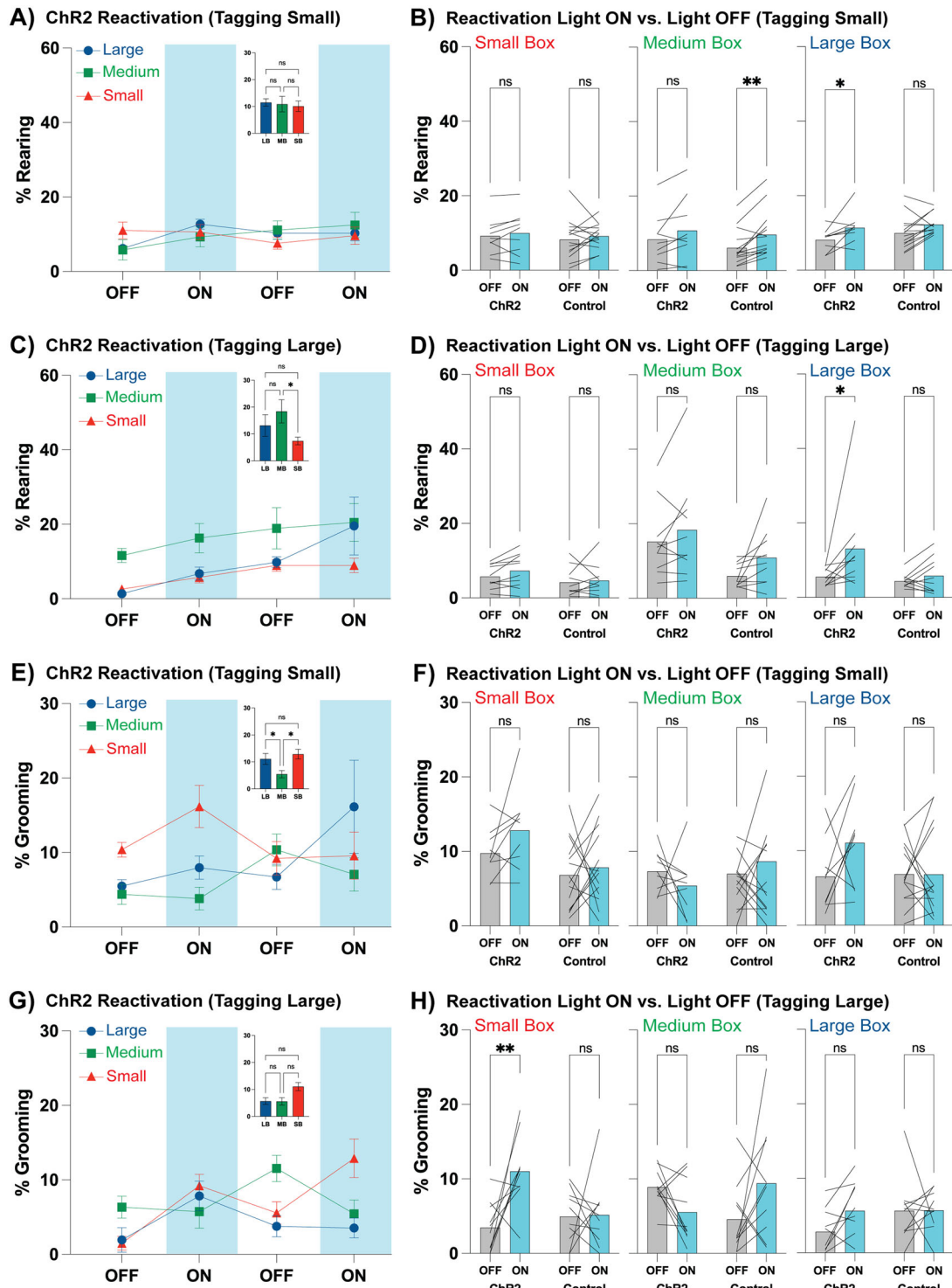


**Figure 4.** Hippocampal CFC engram manipulation differentially alters rearing and grooming behavior across environments. **A**, % Rearing levels for all ChR2 animals conditioned in the small chamber ( $n = 9$ ) binned across 2 min epochs during CFC engram reactivation sessions across all three environments. On average, there was no significant difference in the amount of light-induced rearing during light-ON across all three environments (inset). **B**, Average % rearing across light epochs was compared within ChR2 ( $n = 9$ ) and control ( $n = 14$ ) animals that were conditioned in the small chamber across reactivation environments. **C**, % Rearing levels for all ChR2 animals conditioned in the large chamber ( $n = 10$ ) binned across 2 min epochs during CFC engram reactivation sessions across all three environments. On average, there was a trending, but nonsignificant, difference in light-induced rearing during light-ON across reactivation environments with *post hoc* comparisons revealing a difference in rearing in the SB and MB (inset). **D**, Average % rearing across light epochs was compared within ChR2 ( $n = 10$ ) and control ( $n = 10$ ) animals that were conditioned in the large chamber across reactivation environments. **E**, % Grooming levels for all ChR2 animals conditioned in the small chamber ( $n = 9$ ) binned across 2 min epochs during CFC engram reactivation sessions across all three environments. On average, there was a significant difference in the amount of grooming during light-ON in the SB and LB when compared to the MB (inset). **F**, Average % grooming across light epochs was compared within ChR2 ( $n = 9$ ) and control ( $n = 14$ ) animals that were conditioned in the small chamber across reactivation environments. **G**, % Grooming levels for all ChR2 animals conditioned in the large chamber ( $n = 10$ ) binned across 2 min epochs during CFC engram reactivation sessions across all three environments. On average, there was no difference in grooming during light-ON across all three reactivation environments (inset). **H**, Average % grooming across light epochs was compared within ChR2 ( $n = 10$ ) and control ( $n = 10$ ) animals that were conditioned in the large chamber across reactivation environments. Data are presented as mean  $\pm$  SEM. Significant differences are reported as \*\* $p < 0.01$  and \* $p < 0.05$ .

interaction,  $F_{(1,21)} = 0.4055$ ,  $p = 0.5311$ ; virus condition,  $F_{(1,21)} = 0.9853$ ,  $p = 0.3322$ ; light,  $F_{(1,21)} = 12.30$ ,  $p = 0.0021$ ; ChR2 OFF vs ON,  $p = 0.0294$ ; control OFF vs ON,  $p = 0.0634$ ; Fig. 4B).

For the ChR2 animals conditioned in the large chamber, there was a significant effect from both the reactivation environment and light terms, but no significant interaction between the two (RM two-way ANOVA with a Geisser–Greenhouse correction; interaction,  $F_{(1,888,16.99)} = 1.052$ ,  $p = 0.3670$ ; environment,  $F_{(1,384,12.46)} = 4.976$ ,  $p = 0.0355$ ; light,  $F_{(1,503,13.53)} = 6.962$ ,  $p = 0.0123$ ; Fig. 4C). When light-ON epochs were further averaged, there was a trending difference across the environments, with *post hoc* comparisons yielding a difference in light-induced rearing in the SB when compared to the MB (RM one-way ANOVA with a Geisser–Greenhouse correction and Tukey's multiple comparisons;  $F_{(1,584,14.26)} = 2.972$ ,  $p = 0.0922$ ; LB vs MB,  $p = 0.6274$ ; LB vs SB,  $p = 0.3812$ ; MB vs SB,  $p = 0.0365$ ; Fig. 4C, inset). When compared with control animals conditioned in the large chamber, there was no significant difference in % rearing in the SB (RM two-way ANOVA with a Geisser–Greenhouse correction and Sidak's multiple comparisons; interaction,  $F_{(1,18)} = 0.5455$ ,  $p = 0.4697$ ; virus condition,  $F_{(1,18)} = 1.586$ ,  $p = 0.2240$ ; light,  $F_{(1,18)} = 1.885$ ,  $p = 0.1867$ ; ChR2 OFF vs ON,  $p = 0.2822$ ; control OFF vs ON,  $p = 0.8838$ ); a significant effect from the virus condition and the light, but no interaction between the two terms with *post hoc* mean row comparisons yielding a trending, but nonsignificant, difference in % rearing in control animals in the MB (RM two-way ANOVA with a Geisser–Greenhouse correction and Sidak's multiple comparisons; interaction,  $F_{(1,18)} = 0.3045$ ,  $p = 0.5859$ ; virus condition,  $F_{(1,18)} = 4.778$ ,  $p = 0.0423$ ; light,  $F_{(1,18)} = 5.798$ ,  $p = 0.0270$ ; ChR2 OFF vs ON,  $p = 0.3693$ ; control OFF vs ON,  $p = 0.0990$ ); and a trending, but nonsignificant, effect of virus condition and a significant effect of light-ON % rearing, with *post hoc* comparisons yielding a difference in % rearing in ChR2 animals across light in the LB (RM two-way ANOVA with a Geisser–Greenhouse correction and Sidak's multiple comparisons; interaction,  $F_{(1,18)} = 2.349$ ,  $p = 0.1427$ ; virus condition,  $F_{(1,18)} = 3.019$ ,  $p = 0.0994$ ; light,  $F_{(1,18)} = 5.168$ ,  $p = 0.0355$ ; ChR2 OFF vs ON,  $p = 0.0296$ ; control OFF vs ON,  $p = 0.8454$ ; Fig. 4D). When we quantified % grooming behavior in ChR2 animals conditioned in the small chamber, we found a significant interaction between light and reactivation environment, but not from the individual terms (RM two-way ANOVA with a Geisser–Greenhouse correction; interaction,  $F_{(3,023,24.18)} = 3.141$ ,  $p = 0.0434$ ; environment,  $F_{(1,313,10.50)} = 2.690$ ,  $p = 0.1256$ ; light,  $F_{(1,351,10.81)} = 1.060$ ,  $p = 0.3507$ ; Fig. 4E). When light-ON epochs were averaged together, we found that ChR2 mice groomed more in the LB and SB in comparison to the MB (RM one-way ANOVA with a Geisser–Greenhouse correction and Tukey's multiple comparisons;  $F_{(1,675,13.40)} = 11.57$ ,  $p = 0.0017$ ; LB vs MB,  $p = 0.0200$ ; LB vs SB,  $p = 0.3870$ ; MB vs SB,  $p = 0.0108$ ; Fig. 4E, inset). When compared with control animals conditioned in the small chamber, there was a significant effect of the virus condition in the SB, but no difference across light or an interaction (RM two-way ANOVA with a Geisser–Greenhouse correction and Sidak's multiple comparisons; interaction,  $F_{(1,21)} = 0.5058$ ,  $p = 0.4848$ ; virus condition,  $F_{(1,21)} = 7.912$ ,  $p = 0.0104$ ; light,  $F_{(1,21)} = 2.065$ ,  $p = 0.1654$ ; ChR2 OFF vs ON,  $p = 0.3327$ ; control OFF vs ON,  $p = 0.8134$ ) and no significant effect in MB (RM two-way ANOVA with a Geisser–Greenhouse correction and Sidak's multiple comparisons; interaction,  $F_{(1,21)} = 1.531$ ,  $p = 0.2296$ ; virus condition,  $F_{(1,21)} = 0.4117$ ,  $p = 0.5280$ ; light,  $F_{(1,21)} = 0.008312$ ,  $p = 0.9282$ ; ChR2 OFF vs ON,  $p = 0.6450$ ; control OFF vs ON,  $p = 0.6031$ ) or LB (RM two-way

ANOVA with a Geisser–Greenhouse correction and Sidak's multiple comparisons; interaction,  $F_{(1,21)} = 2.213$ ,  $p = 0.1517$ ; virus condition,  $F_{(1,21)} = 1.411$ ,  $p = 0.2481$ ; light,  $F_{(1,21)} = 2.205$ ,  $p = 0.1525$ ; ChR2 OFF vs ON,  $p = 0.1362$ ; control OFF vs ON,  $p = 0.9999$ ; Fig. 4F). For ChR2 animals conditioned in the large chamber, there was a trending effect of light and a significant effect of the reactivation environment and an interaction between light and reactivation environment on % grooming (RM two-way ANOVA with a Geisser–Greenhouse correction; interaction,  $F_{(3,350,30.15)} = 4.262$ ,  $p = 0.0105$ ; environment,  $F_{(1,553,13.97)} = 7.049$ ,  $p = 0.0110$ ; light,  $F_{(1,738,15.64)} = 3.516$ ,  $p = 0.0601$ ; Fig. 4G). When the light-ON epochs were further averaged together, we found no statistical differences in % grooming across reactivation environments (RM one-way ANOVA with a Geisser–Greenhouse correction and Tukey's multiple comparisons;  $F_{(1,940,17.46)} = 1.075$ ,  $p = 0.3610$ ; LB vs MB,  $p = 0.9962$ ; LB vs SB,  $p = 0.5109$ ; MB vs SB,  $p = 0.4293$ ; Fig. 4G, inset). Lastly, when compared with control animals conditioned in the large chamber, there was a significant effect of virus condition, light, and an interaction between the two terms in the SB with *post hoc* mean row comparisons finding a significant increase in grooming in ChR2 during light-ON (RM two-way ANOVA with a Geisser–Greenhouse correction and Sidak's multiple comparisons; interaction,  $F_{(1,18)} = 4.996$ ,  $p = 0.0383$ ; virus condition,  $F_{(1,18)} = 5.998$ ,  $p = 0.0248$ ; light,  $F_{(1,18)} = 5.614$ ,  $p = 0.0292$ ). There was a significant interaction of the virus condition and light in the MB (RM two-way ANOVA with a Geisser–Greenhouse correction and Sidak's multiple comparisons; interaction,  $F_{(1,18)} = 5.843$ ,  $p = 0.0265$ ; virus condition,  $F_{(1,18)} = 0.02054$ ,  $p = 0.8876$ ; light,  $F_{(1,18)} = 0.2003$ ,  $p = 0.6598$ ; ChR2 OFF vs ON,  $p = 0.3287$ ; control OFF vs ON,  $p = 0.1124$ ), but no significance in the LB (RM two-way ANOVA with a Geisser–Greenhouse correction and Sidak's multiple comparisons; interaction,  $F_{(1,18)} = 1.561$ ,  $p = 0.2276$ ; virus condition,  $F_{(1,18)} = 1.556$ ,  $p = 0.2282$ ; light,  $F_{(1,18)} = 1.703$ ,  $p = 0.2083$ ; ChR2 OFF vs ON,  $p = 0.1676$ ; control OFF vs ON,  $p = 0.9990$ ; Fig. 4H). This points to the intriguing idea that hippocampal engrams are not fixed to produce a singular behavioral phenotype during optogenetic reactivation. Together, these data suggest that the same population of DG cells is capable of differentially driving behavioral responses in a manner contingent on the physical environment itself.

### Engram reactivation in the SB increases brain-wide cFos density

We next sought to measure brain-wide correlates of hippocampal CFC engram reactivation. Prior work suggests that artificially reactivating hippocampal engrams increases cFos expression in downstream areas that are implicated in mediating learning and affective states (Ramirez et al., 2015; Roy et al., 2022). We hypothesized that we would see significant differences in cFos expression in these regions as well as candidate regions that dictate behavioral outputs. In separate sets of animals, we tagged a hippocampal CFC engram in the small operant chamber, but mice were subjected to only 1 d of reactivation in either the SB or the LB (Fig. 5A). We sacrificed animals 90 min after the last light-ON epoch to capture endogenous cFos expression and sent brain tissue for whole organ clearing, immunohistochemistry, light-sheet microscopy, and cell quantification (LifeCanvas Technologies; see Methods). We first recapitulated light-induced freezing in ChR2 animals in the SB condition (RM two-way ANOVA with Sidak's multiple comparisons for a mean row effect; interaction,  $F_{(1,14)} = 10.62$ ,  $p = 0.0057$ ; virus condition,  $F_{(1,14)} = 3.785$ ,  $p = 0.0721$ ; light epoch,  $F_{(1,14)} = 2.155$ ,  $p = 0.1643$ ;

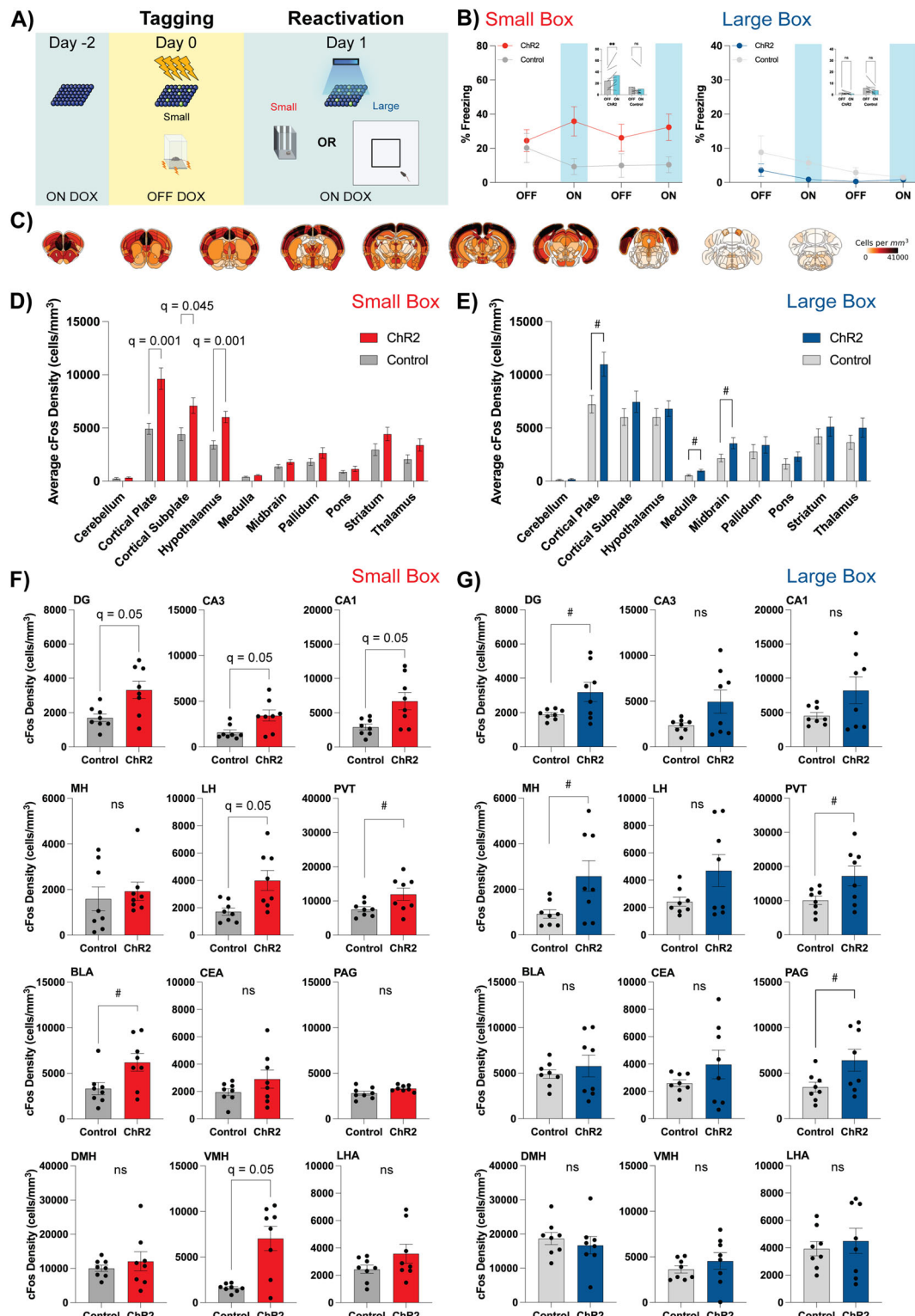


**Figure 5.** Engram reactivation in the SB increases brain-wide cFos density in areas mediating memory and behavior. **A**, Schematic of the experimental paradigm. Animals experience activity-dependent tagging of a CFC engram, but reactivation for only 1 d after the DOX window is closed. They are perfused 90 min after the last light-ON epoch to capture peak endogenous cFos expression. **B**, % Freezing levels for Chr2 animals ( $n = 8$ ) and control animals ( $n = 8$ ) for the SB condition across light epochs. There is a significant increase in the amount of light-induced freezing in only Chr2 animals (inset). % Freezing for separate groups of Chr2 animals ( $n = 8$ ) and control animals ( $n = 8$ ) for the LB condition across light epochs. There is no difference in the amount of freezing of the chamber across groups (inset). \*\* $p < 0.01$ . **C**, Example heatmap of rodent brain-wide cFos density ( $\text{cells}/\text{mm}^3$ ) from a ChR2-injected animal in the SB condition. **D**, Aggregation of the average cFos density in 10 parent brain areas registered to the Allen Brain Atlas in the SB condition. The observed  $q$ -values that are considered “discoveries” after the FDR correction are reported. **E**, Aggregation of the average cFos density in 10 parent brain areas registered to the Allen Brain Atlas in the LB condition. The observed  $q$ -values that are considered “discoveries” after the FDR correction are reported. **F**, cFos density for 12 individual ROIs were compared between Chr2 and Control animals in the SB condition using multiple unpaired Welch-corrected  $t$  tests with a Benjamini–Hochberg correction of 5%. Observed  $q$ -values that are considered discoveries after the FDR are reported. **G**, cFos density for 12 individual ROIs were compared between Chr2 and Control animals in the LB condition using multiple unpaired Welch-corrected  $t$  tests corrected with a Benjamini–Hochberg correction of 5%. Data are presented as mean  $\pm$  SEM. In all panels, # is indicative of statistical significance before the FDR correction was applied, yet failed to be considered an FDR-corrected discovery.

ChR2 OFF vs ON,  $p = 0.0097$ ; control OFF vs ON,  $p = 0.4012$ ; Fig. 5*B*, inset), but saw no changes in freezing in the LB condition (RM two-way ANOVA with a Geisser–Greenhouse correction and Sidak's multiple comparisons for a mean row effect; interaction,  $F_{(1,14)} = 0.9747$ ,  $p = 0.3403$ ; virus condition,  $F_{(1,14)} = 7.348$ ,  $p = 0.0169$ ; light epoch,  $F_{(1,14)} = 4.189$ ,  $p = 0.0599$ ; ChR2 OFF vs ON,  $p = 0.7151$ ; control OFF vs ON,  $p = 0.0974$ ; Fig. 5*B*, inset). We assessed endogenous cFos density in 147 regions spanning anterior cortical areas to the posterior hindbrain and assigned each to a respective “parent brain region” from the Allen Brain Atlas (e.g., cortical plate, midbrain; Fig. 5*C*, Table 1; Oh et al., 2014). We first examined average cFos density across 10 parent regions under each environmental condition. In the SB, where there was light-induced freezing (Fig. 5*B*, left), we observed corresponding differences in the cortical plate ( $t = 4.147$ ,  $p = 0.002$ ), cortical subplate ( $t = 2.835$ ,  $p = 0.0137$ ), and hypothalamus ( $t = 3.977$ ,  $p = 0.002$ ) in the ChR2 group [multiple  $t$  tests with 5% Benjamini–Hochberg FDR (Benjamini and Hochberg, 1995; Glickman et al., 2014); Fig. 5*D*]. Conversely in the LB condition, where we saw no alterations in behavior (Fig. 5*B*, right), there were statistically significant differences in cFos density in the cortical plate ( $t = 2.676$ ,  $p = 0.01$ ), medulla ( $t = 3.125$ ,  $p = 0.04$ ), and midbrain ( $t = 2.228$ ,  $p = 0.031$ ) in the respective ChR2 group, but they did not survive the FDR correction (multiple  $t$  tests with 5% Benjamini–Hochberg FDR; Fig. 5*E*). This supports the notion that optogenetic reactivation of a hippocampal engram is sufficient to drive cFos expression in a brain-wide pattern that itself depends on the environment in which stimulation occurred.

Next, we examined cFos density by individual brain regions. We honed in on twelve individual regions that have been heavily implicated in driving memory and defensive behaviors, specifically the hippocampus (DG, CA3, CA1; Scoville and Milner, 1957; Fanselow and Dong, 2010), amygdala (BLA, CEA; Amano et al., 2011; Herry and Johansen, 2014; Yu et al., 2016; Fadok et al., 2017), habenula (LH, MH; Pobbe and Zangrossi, 2010; Stamatakis and Stuber, 2012; Soria-Gómez et al., 2015; Zhang et al., 2016), paraventricular nucleus of the thalamus (PVT; Do-Monte et al., 2015; Penzo et al., 2015; Ma et al., 2021), periaqueductal gray (PAG; Deng et al., 2016; Tovote et al., 2016), and hypothalamus (DMH, VMH, LHA; Jardim and Guimarães, 2004; Lin et al., 2011; Kim et al., 2013; Jimenez et al., 2018). We predicted that these systems would be differentially engaged across conditions as a result of hippocampal CFC engram reactivation. In the SB condition, where we observed light-induced freezing (Fig. 5*B*, left), we found that there were significant differences in cFos density in the DG ( $t = 2.987$ ,  $p = 0.014$ ), CA3 ( $t = 2.779$ ,  $p = 0.020$ ), CA1 ( $t = 2.822$ ,  $p = 0.021$ ), LH ( $t = 2.926$ ,  $p = 0.017$ ), and VMH ( $t = 4.043$ ,  $p = 0.005$ ) even after applying a 5% FDR correction (Fig. 5*F*). In the LB condition, we found statistically significant differences in cFos expression in the DG ( $t = 2.317$ ,  $p = 0.05$ ), MH ( $t = 2.391$ ,  $p = 0.043$ ), PVT ( $t = 2.271$ ,  $p = 0.048$ ), and PAG ( $t = 2.232$ ,  $p = 0.05$ ); however, these comparisons did not survive the FDR correction (Fig. 5*G*). Finally, we compared cFos density in the DG across all experimental conditions and found significant variation from the virus condition, but not from the reactivation environment or an interaction between the two (two-way ANOVA with a Geisser–Greenhouse correction; interaction,  $F_{(1,28)} = 0.1748$ ,  $p = 0.6791$ ; virus condition,  $F_{(1,28)} = 14.01$ ,  $p = 0.0008$ ; environment,  $F_{(1,28)} = 0.0069$ ,  $p = 0.9341$ ). However, *post hoc* comparisons revealed that both ChR2 groups had similar cFos expression, and ChR2 animals had significantly higher cFos

**Table 1. List of 147 brain regions examined in this study. Regions are organized alphabetically and have their acronyms as well as Parent Region listed**

Brain region	Abbreviation	Parent region
Anterior amygdalar area	AAA	Striatum
Anterior cingulate area	ACA	Cortical plate
Nucleus accumbens	ACB	Striatum
Anterior hypothalamic nucleus	AHN	Hypothalamus
Agranular insular area	AI	Cortical plate
Anterior tegmental nucleus	AT	Midbrain
Auditory areas	AUD	Cortical plate
Anteroventral preoptic nucleus	AVP	Hypothalamus
Anteroventral periventricular nucleus	AVPV	Hypothalamus
Bed nucleus of the anterior commissure	BAC	Pallidum
Basolateral amygdala	BLA	Cortical subplate
Basomedial amygdala	BMA	Cortical subplate
Bed nuclei of the stria terminalis	BST	Pallidum
Field CA1	CA1	Cortical plate
Field CA2	CA2	Cortical plate
Field CA3	CA3	Cortical plate
Central amygdalar nucleus	CEA	Cortical subplate
Central lateral nucleus of the thalamus	CL	Thalamus
Clastrum	CLA	Cortical subplate
Central linear nucleus raphe	CLI	Midbrain
Central medial nucleus of the thalamus	CM	Thalamus
Caudoputamen	CP	Striatum
Superior central nucleus raphe	CS	Pons
Cuneiform nucleus	CUN	Midbrain
Dentate gyrus	DG	Cortical plate
Dorsomedial nucleus of the hypothalamus	DMH	Hypothalamus
Denate nucleus	DN	Cerebellum
Dorsal nucleus raphe	DR	Midbrain
Ectorhinal area	ECT	Cortical plate
Entorhinal area	ENT	Cortical plate
Endopiriform nucleus	EP	Cortical subplate
Edinger–Westphal nucleus	EW	Midbrain
Fasciola cinerea	FC	Cortical plate
Fastigial nucleus	FN	Cerebellum
Fundus of striatum	FS	Striatum
Globus pallidus, external segment	GPe	Pallidum
Globus pallidus, internal segment	GPi	Pallidum
Gustatory areas	GU	Cortical plate
Hemispheric regions	HEM	Cerebellum
Intercalated amygdalar nucleus	IA	Striatum
Inferior colliculus	IC	Midbrain
Interfascicular nucleus raphe	IF	Midbrain
Induseum griseum	IG	Cortical plate
Infralimbic area	ILA	Cortical plate
Interposed nucleus	IP	Cerebellum
Interpeduncular nucleus	IPN	Midbrain
Lateral amygdalar nucleus	LA	Cortical subplate
Locus ceruleus	LC	Pons
Lateral dorsal nucleus of thalamus	LD	Thalamus
Lateral habenula	LH	Thalamus
Lateral hypothalamic area	LHA	Hypothalamus
Lateral preoptic area	LPO	Hypothalamus
Lateral septal nucleus	LS	Striatum
Magnocellular nucleus	MA	Pallidum
Medial accessory oculomotor nucleus	MA3	Midbrain
Mammillary body	MBO	Hypothalamus
Mediodorsal nucleus of the thalamus	MD	Thalamus
Median eminence	ME	Hypothalamus
Medial amygdalar nucleus	MEA	Cortical subplate
Median preoptic nucleus	MEPO	Hypothalamus
Midbrain trigeminal nucleus	MEV	Midbrain
Medial habenula	MH	Thalamus
Somatotmotor areas	MO	Cortical plate
Medial preoptic nucleus	MPN	Hypothalamus

(Table continues.)

**Table 1. Continued**

Brain region	Abbreviation	Parent region
Medial preoptic area	MPO	Hypothalamus
Midbrain reticular nucleus	MRN	Midbrain
Medial septal nucleus	MS	Pallidum
Medulla, motor related	MY-mot	Medulla
Medulla, behavioral state related	MY-sat	Medulla
Medulla, sensory related	MY-sen	Medulla
Nucleus of the brachium of the inferior colliculus	NB	Midbrain
Diagonal band nucleus	NDB	Pallidum
Olfactory areas	OLF	Cortical plate
Orbital area	ORB	Cortical plate
Olfactory tubercle	OT	Striatum
Vascular organ and of the lamina terminalis	OV	Hypothalamus
Pons, motor related	P-mot	Pons
Pons, behavioral state related	P-sat	Pons
Pons, sensory related	P-sen	Pons
Posterior amygdalar nucleus	PA	Cortical subplate
Periaqueductal gray	PAG	Midbrain
Parasubiculum	PAR	Cortical plate
Parabrachial nucleus	PB	Pons
Parabigeminal nucleus	PBG	Midbrain
Paracentral nucleus	PCN	Thalamus
Posterodorsal preoptic nucleus	PD	Hypothalamus
Perirhinal area	PERI	Cortical plate
Parafascicular nucleus	PF	Thalamus
Posterior hypothalamic nucleus	PH	Hypothalamus
Prelimbic area	PL	Cortical plate
Dorsal premammillary nucleus	PMd	Hypothalamus
Ventral premammillary nucleus	PMv	Hypothalamus
Paranigral nucleus	PN	Midbrain
Postsubiculum	POST	Cortical plate
Peripeduncular nucleus	PP	Thalamus
Pedunculopontine nucleus	PPN	Midbrain
Perireunensis nucleus	PR	Thalamus
Presubiculum	PRE	Cortical plate
Pretectal region	PRT	Midbrain
Parastrial nucleus	PS	Hypothalamus
Preparasubthalamic nucleus	PST	Hypothalamus
Parasubthalamic nucleus	PSTN	Hypothalamus
Posterior parietal association areas	PTLp	Cortical plate
Paraventricular nucleus of the thalamus	PVT	Thalamus
Periventricular zone	PVZ	Hypothalamus
Perifornical nucleus	PeF	Hypothalamus
Prosubiculum	ProS	Cortical plate
Retrochiasmatic area	RCH	Hypothalamus
Nucleus of reunions	RE	Thalamus
Rhomboid nucleus	RH	Thalamus
Rostral linear nucleus raphe	RL	Midbrain
Red nucleus	RN	Midbrain
Midbrain reticular nucleus, retrorubral area	RR	Midbrain
Retrosplenial area	RSP	Cortical plate
Reticular nucleus of the thalamus	RT	Thalamus
Nucleus sagulum	SAG	Midbrain
Subparaventricular zone	SBPV	Hypothalamus
Suprachiasmatic nucleus	SCH	Hypothalamus
Superior colliculus, motor related	SCm	Midbrain
Superior colliculus, sensory related	SCs	Midbrain
Septofimbrial nucleus	SF	Striatum
Subfornical organ	SFO	Hypothalamus
Septohippocampal nucleus	SH	Striatum
Substantia innominata	SI	Pallidum
Substantia nigra, compact part	SNC	Midbrain
Substantia nigra, reticular part	SNr	Midbrain
Subparafascicular area	SPA	Thalamus
Subparafascicular nucleus	SPF	Thalamus
Somatosensory areas	SS	Cortical plate

(Table continues.)

**Table 1. Continued**

Brain region	Abbreviation	Parent region
Subthalamic nucleus	STN	Hypothalamus
Subiculum	SUB	Cortical plate
Temporal association areas	TEa	Cortical plate
Triangular nucleus of the septum	TRS	Pallidum
Tuberous nucleus	TU	Hypothalamus
Ventral anterolateral complex of the thalamus	VAL	Thalamus
Vermal regions	VERM	Cerebellum
Visual areas	VIS	Cortical plate
Visceral area	VISC	Cortical plate
Ventrolateral preoptic nucleus	VLPO	Hypothalamus
Ventral medial nucleus of the thalamus	VM	Thalamus
Ventromedial hypothalamic nucleus	VMH	Hypothalamus
Ventromedial preoptic nucleus	VMPO	Hypothalamus
Ventral posterior complex of the thalamus	VP	Thalamus
Ventral tegmental area	VTA	Midbrain
Ventral tegmental nucleus	VTN	Midbrain
Vestibulocerebellar nucleus	VeCB	Cerebellum
Zona incerta	ZI	Hypothalamus

density than their respective Controls in the SB reactivation environment, yet there was a trending, but nonsignificant, difference in cFos density across groups in the LB (Tukey's multiple comparisons; ChR2 SB vs LB,  $p = 0.9952$ ; control SB vs LB,  $p = 0.9844$ ; ChR2 SB vs control SB,  $p = 0.0310$ ; ChR2 LB vs control LB,  $p = 0.1106$ ; Fig. 6A). Additionally, during hippocampal CFC engram reactivation in the SB, we found a positive linear relationship between freezing and DG cFos density in ChR2 animals that was not seen in Control animals (Fig. 6B). The observed freezing behavior in ChR2 animals is further corroborated by significant engram overlap with endogenous cFos (Fig. 6C). This suggests that hippocampal CFC engram reactivation engages the DG as well as downstream areas that mediate memory and behavioral expression that is also contingent on the animal's environment.

### Hippocampal CFC engram reactivation alters brain-wide cFos correlations

We hypothesized that environmental contingencies and hippocampal CFC engram reactivation would both induce an effect on brain-wide cFos expression. To test this, we first visualized interregional Spearman's correlations for all conditions and organized them based on the parent region in the Allen Brain Atlas (Fig. 7F). To determine how engram reactivation altered cFos correlation, we used a nonparametric permutation test that quantified the absolute mean difference in cFos correlation. We observed greater Spearman correlation coefficients in the ChR2 SB condition in comparison to the Control SB condition ( $p = 0.0$ , stat = 0.15812; Fig. 7A,B). We also found that in the ChR2 LB condition, there were also larger Spearman coefficients in comparison to their respective control group ( $p = 0.0$ , stat = 0.15819; Fig. 7D,E). This suggests that the ChR2 activation, regardless of the environmental variable, increased the mean correlation coefficient. We then determined if the environmental condition was capable of affecting the overall connectivity of the brain. To test this, we compared the correlation coefficient distributions across environmental conditions within the same treatment. We found that the control groups were significantly different from one another ( $p = 0.0$ , stat = 0.04778). The experimental groups were also significantly different from one another ( $p = 0.0$ , stat = 0.04879). Lastly, we determined which conditions were different from a group of animals that

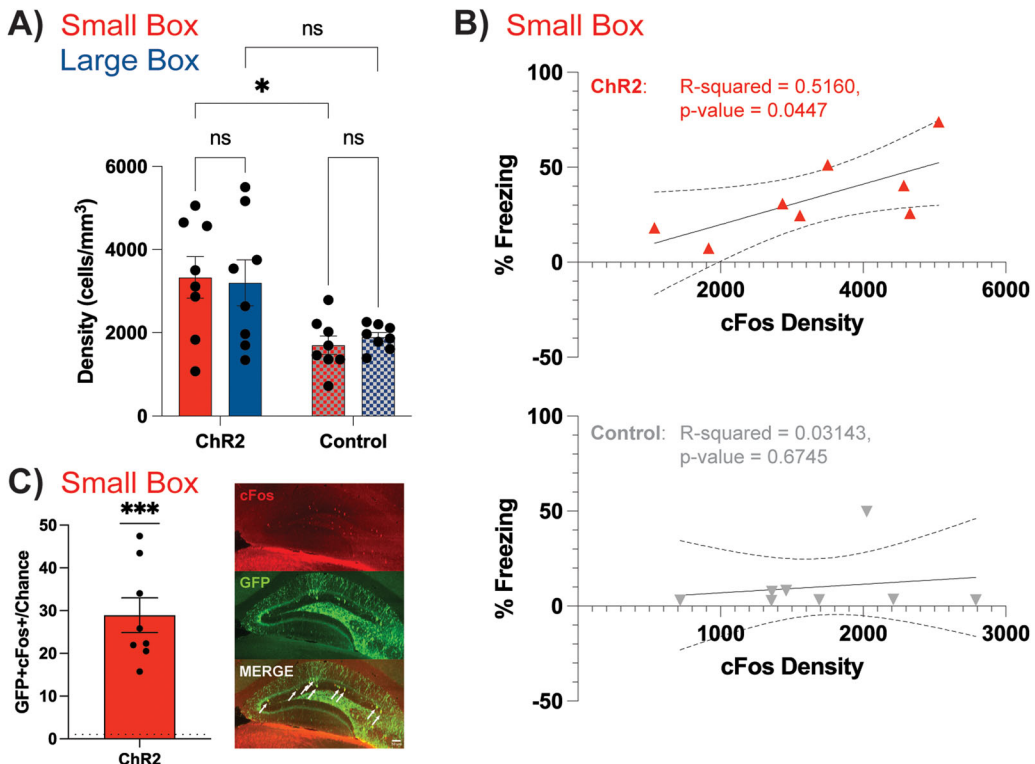


**Figure 6.** Enhanced DG cFos density in ChR2 SB animals relates to light-induced freezing. **A**, cFos density measurements in the DG in ChR2 and Control animals across both the SB and the LB ( $n = 8$  animals/group). \* $p < 0.05$ . **B**, Linear regression analyses comparing cFos density expression to % freezing during hippocampal CFC engram reactivation in the SB condition. There is a positive relationship between DG cFos and % freezing only in ChR2 animals (top) that is not observed in control animals (bottom). **C**, Ensemble overlap between endogenous cFos and the ChR2-eYFP engram is greater than chance in ChR2 SB animals ( $n = 8$ ) as revealed by a one-sample  $t$  test ( $t = 6.860$ ,  $p = 0.0002$ ). Representative images of endogenous cFos (red), the tagged hippocampal CFC engram (green), and ensemble overlap (merge, arrows) (right). The scale bar represents 50  $\mu$ m.

underwent CFC but natural fear memory retrieval in lieu of engram reactivation (i.e., natural retrieval). To do this, we compared all conditions to the natural retrieval group and found that all were significantly different (control LB,  $p = 0.0$ , stat = 0.06912; control SB,  $p = 0.0$ , stat = 0.02134; ChR2 SB,  $p = 0.0$ , stat = 0.1795; ChR2 LB,  $p = 0.0$ , stat = 0.2273; Fig. 7G). Overall, this analysis suggests that both the environment and our engram perturbation create unique patterns of brain activity. Next, we used uniform manifold approximation and projection (UMAP; McInnes et al., 2020), a nonlinear dimensionality reduction technique to represent the correlation matrices' values in two-dimensional space. We used UMAP to test whether the Spearman coefficients would segregate by brain region or by experimental condition. We found that the correlation coefficients were clustered by the experimental condition, irrespective of the parent brain region (Fig. 7H,I). Notably, while the control conditions were the closest in terms of their centers of mass, the ChR2 conditions clustered away from each other. Interestingly, the natural retrieval group, while producing similar levels of freezing to the ChR2 SB group (Fig. 8), clustered nearby both control conditions. This suggests that the optogenetic perturbation of a hippocampal CFC engram causes brain-wide changes that are unique to natural fear retrieval. Furthermore, we see that all of the clusters are well defined, which helps explain why in our previous statistical tests, all conditions were significantly different from one another, and that each experimental group displayed unique patterns of cFos correlation. This lends credence to the idea that our environmental and engram manipulations create distinct brain states.

### Unique modular structures are observed across engram reactivation and environmental conditions

To understand the brain-wide interactions and functional pairwise relationships that occur during our engram manipulation, we constructed and analyzed cFos cell density networks using graph theory via a custom pipeline freely available on GitHub (see Methods). We defined graphs to include only Spearman correlations that survived a 5% FDR correction (Fig. 9A,C). We wanted to understand to what extent the brain, especially in fear memory states, forms a modular structure. In network analysis, communities (i.e., modules) are subsets of nodes within a network that are more connected amongst themselves than with other subsets of nodes (Fortunato and Newman, 2022). One of the most popular algorithms for community detection is the Louvain algorithm (Blondel et al., 2008), but recent work showed that this algorithm can yield arbitrarily connected modules (Traag et al., 2019). To overcome this issue, we utilized the Leiden community detection method (Traag et al., 2019). After applying this algorithm, we found that the modular compositions varied across experimental conditions and environments. Qualitatively, networks that were generated from the experimental groups [i.e., received optogenetic stimulation (ChR2)] exhibited different structural features, such as the number of edges, islands (i.e., nodes with a degree measure of zero), and modules (Fig. 10). It is important to note that these data are observational in nature and as such are descriptive as presented.

When examining the composition of brain regions within modules, we observed that there was one large module that contained many hippocampal, thalamic, and hypothalamic nuclei in

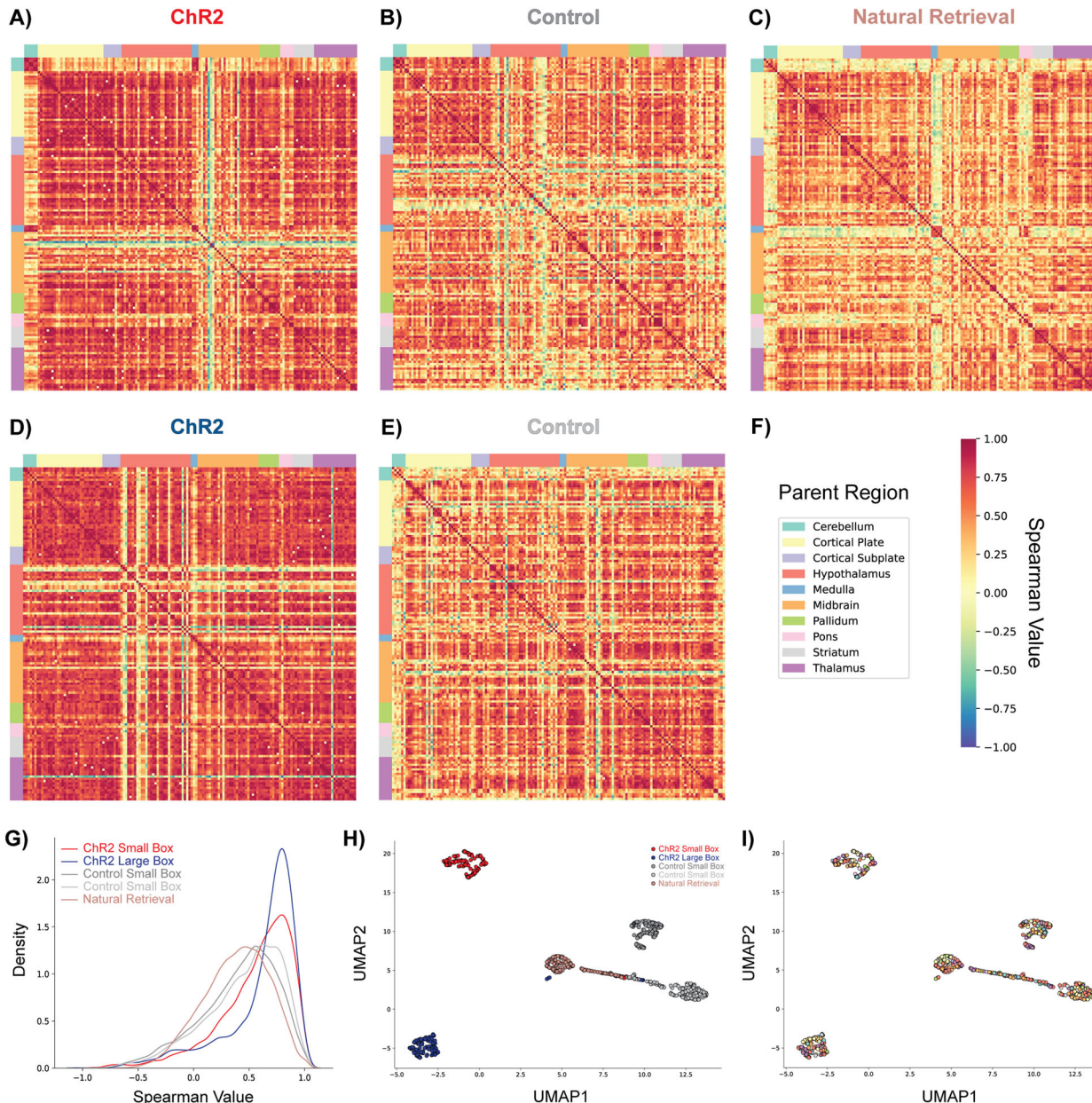


**Figure 7.** Hippocampal CFC engram reactivation differentially increases cFos correlations across environments. **A**, cFos interregional Spearman's correlation matrix generated from ChR2 SB ( $n = 8$ ) animals across 147 brain ROIs organized by anatomical location (Table 1). Warmer colors are indicative of more positive correlations and cooler colors for more negative correlations. **B**, cFos interregional Spearman's correlation matrix generated from control SB ( $n = 8$ ) animals across 147 brain ROIs organized by anatomical location (Table 1). Warmer colors are indicative of more positive correlations and cooler colors for more negative correlations. **C**, cFos interregional Spearman's correlation matrix generated from the natural retrieval group ( $n = 12$ ) across 147 brain ROIs organized by anatomical location (Table 1). Warmer colors are indicative of more positive correlations and cooler colors for more negative correlations. **D**, cFos interregional Spearman's correlation matrix generated from ChR2 LB ( $n = 8$ ) animals across 147 brain ROIs organized by anatomical location (Table 1). Warmer colors are indicative of more positive correlations and cooler colors for more negative correlations. **E**, cFos interregional Spearman's correlation matrix generated from Control LB ( $n = 8$ ) animals across 147 brain ROIs organized by anatomical location (Table 1). Warmer colors are indicative of more positive correlations and cooler colors for more negative correlations. **F**, Color key (left) for parent regions based on the Allen Brain Atlas (cyan, cerebellum; yellow, cortical plate; lilac, cortical subplate; red, hypothalamus; blue, medulla; orange, midbrain; green, pallidum; pink, pons; gray, striatum; purple, thalamus). Color key (right) for Spearman's correlation values ranging from  $-1$  to  $1$ . Warmer colors (i.e., yellows and reds) are indicative of positive values and cooler colors (i.e., greens and blues) are indicative of negative values. **G**, Distributions of all Spearman's correlation values for all experimental conditions. Both ChR2 SB and ChR2 LB have a greater average Spearman correlation than either the control group or the natural retrieval condition. **H**, UMAP representations of all experimental conditions. Each point in UMAP space represents all cross-correlation values of an individual brain region reduced in two-dimensional space. All conditions are separate in linear space, yet both control groups were closer in space than either of the ChR2 groups, showing that these states are inherently distinct. Additionally, the natural retrieval condition clustered between the ChR2 and control groups. **I**, UMAP representations of brain regions spanning Allen Brain Atlas parent regions. Each point in UMAP space represents all cross-correlation values of an individual brain region reduced in two-dimensional space. Brain regions do not show distinct segregation, as all of these colors are intermingled, suggesting that engram stimulation does not bias particular brain regions into separable linear spaces.

both ChR2 networks. This implies that the thalamus, hypothalamus, and hippocampus are more correlated in their activity after optogenetic stimulation, which is in line with previous findings that demonstrated strong connections across the thalamus and

hippocampus in fear memory networks (Wheeler et al., 2013; Vetere et al., 2017; Silva et al., 2019). Interestingly, only the ChR2 SB group contained the trisynaptic hippocampal circuit (DG, CA1, CA3) within one module, and in the ChR2 LB group,

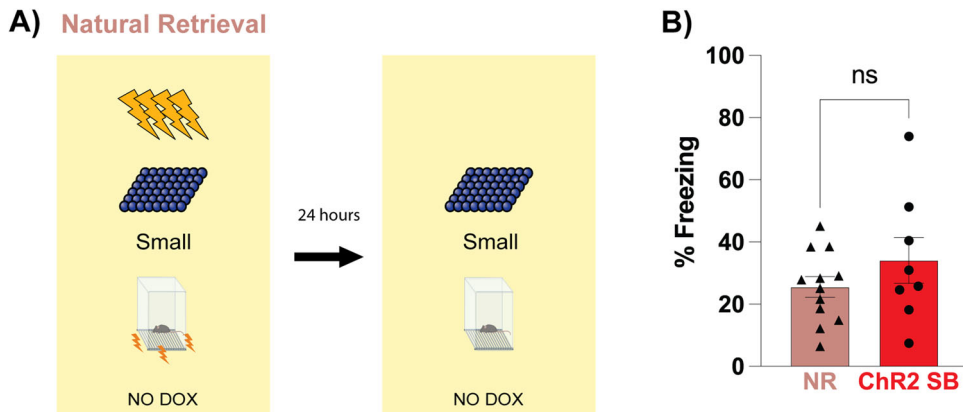


**Figure 8.** Natural retrieval of a fear memory produces similar freezing levels to hippocampal CFC engram reactivation in the SB. **A**, Schematic of the behavioral schedule for a group of naive mice ( $n = 12$ ) that do not have engram tagging and, therefore, do not need to be on the DOX diet. Mice are conditioned as other groups (four shocks, 2 s each, 0.5 mA) and are placed back in the original context in which they got shocked 24 h after CFC for a 3 min retrieval session. **B**, % Freezing levels for the natural retrieval group ( $n = 12$ ) and the average light-ON % freezing levels for all animals conditioned in the small chamber and underwent reactivation in the ChR2 SB condition ( $n = 8$ ). An unpaired  $t$  test determined that the amount of freezing during these two experimental conditions was statistically insignificant ( $t = 1.184$ ,  $p = 0.2519$ ).

the CA1 region was not within the partition containing the remaining trisynaptic circuit. This could possibly be explained by the contextual mismatch of the original fear conditioning chamber and the larger testing arena (Fig. 5A, see Discussion). Interestingly, in the natural retrieval condition, we found that there were dominant thalamic, hypothalamic, and hippocampal modules, which replicated earlier findings by Wheeler et al. (2013) where they saw similar modular structures. We also note that the modules in the natural retrieval network are qualitatively more homogeneous, which could signify the naturalistic aspect of the experiment in comparison to optogenetics which seems to be drastically increasing the correlation between brain regions, especially the hippocampus and regions traditionally associated with fear, such as the BLA. The control networks were most notable for their general connection sparsity and small module sizes (Fig. 10). This is expected, as these mice explored a novel context without hippocampal CFC engram reactivation or naturalistic fear memory retrieval and therefore are not producing fear-related behaviors.

To identify quantitative differences in network composition, we generated degree rank plots across conditions (Fig. 9D). We found a significant difference in the degree rank distribution across ChR2 and control groups in both the SB (KS test:  $D = 0.6735$ ,  $p < 0.0001$ ) and LB (KS test:  $D = 0.7551$ ,  $p < 0.0001$ ). Additionally, we found a significant difference in the degree rank across both ChR2 groups and the natural retrieval group (Kruskal–Wallis test with multiple comparisons, statistic = 102.2,  $p < 0.0001$ ; ChR2 SB vs ChR2 LB,  $p < 0.0001$ ; ChR2 SB vs natural retrieval,  $p < 0.0001$ ; ChR2 LB vs natural retrieval,  $p < 0.0001$ ). Overall, these results are in line with the observation that our hippocampal CFC engram reactivation is creating more correlated brain states. The large change in the LB condition also implies that although we lacked a behavioral phenotype in ChR2-injected animals (Fig. 5B), we are still likely engaging brain-wide fear circuitry with our engram manipulations.

#### Engram reactivation differentially engages network hubs across environmental conditions

Hubs in a network are nodes that are of high importance for signal propagation and are defined using a series of centrality metrics in addition to community-based characteristics when

clustering algorithms are applied (Guimerà and Nunes Amaral, 2005; van den Heuvel and Sporns, 2013). To identify nodes that act as central hubs, we generated a “hub score” by characterizing the node distribution across five centrality metrics: degree centrality, betweenness, closeness, eigenvector centrality, and clustering coefficient (van den Heuvel et al., 2010; Coelho et al., 2018; Fig. 11A). Nodes that fell in the top 20% (or bottom 20% in the case of clustering coefficient) of any of these metrics receive a +1 added to their hub score. Here, we defined central hubs as having a score of 3 or greater. We found 22 central hubs unique to the ChR2 SB network, with many implicated in memory (e.g., DG, ILA, BLA) and behavior (e.g., PVT, LHA; Fig. 11B, top). Interestingly, all three of the shared central hubs between the ChR2 and control SB networks are also implicated in memory-guided actions. We speculate that these hubs may be involved in processing shared representational features of the SB environment through their coordinated activity. There were 26 central hubs in the ChR2 network generated under the LB condition, 17 of which are unique to the network (Fig. 11B, bottom). Importantly, the DG and BLA are two shared hub regions in both ChR2 networks generated from the SB and LB condition, demonstrating that our engram manipulation does engage largely characterized memory systems. Lastly, we identified 24 central hub regions in the natural retrieval network (Fig. 11C). Many of these hub regions were cortical plate and subplate regions implicated in memory-guided actions (i.e., CA1, CA3, BLA) and other thalamic and hypothalamic regions implicated in memory or defensive behavior (i.e., RE, ZI, VMH). Additionally, the natural retrieval and ChR2 SB condition shared hub regions such as the BLA, BMA, PA, ILA, and ACB suggesting that shared behavioral phenotypes (i.e., freezing) can also share hub regions that are implicated in memory and defense systems even though network features do not point to identical brain states, indicating that memory generated fear states can still have differential patterns of brain activity. The BLA and ILA are shared across both ChR2 groups and the natural retrieval group, which also suggests that these regions can become engaged as hubs in the LB during hippocampal CFC engram reactivation without the presence of freezing without the emergence of a freezing-related behavioral phenotype (i.e., in the LB, Fig. 5B). This is further supported by the DG being recruited as a central hub in both ChR2 groups, as this is the site of our

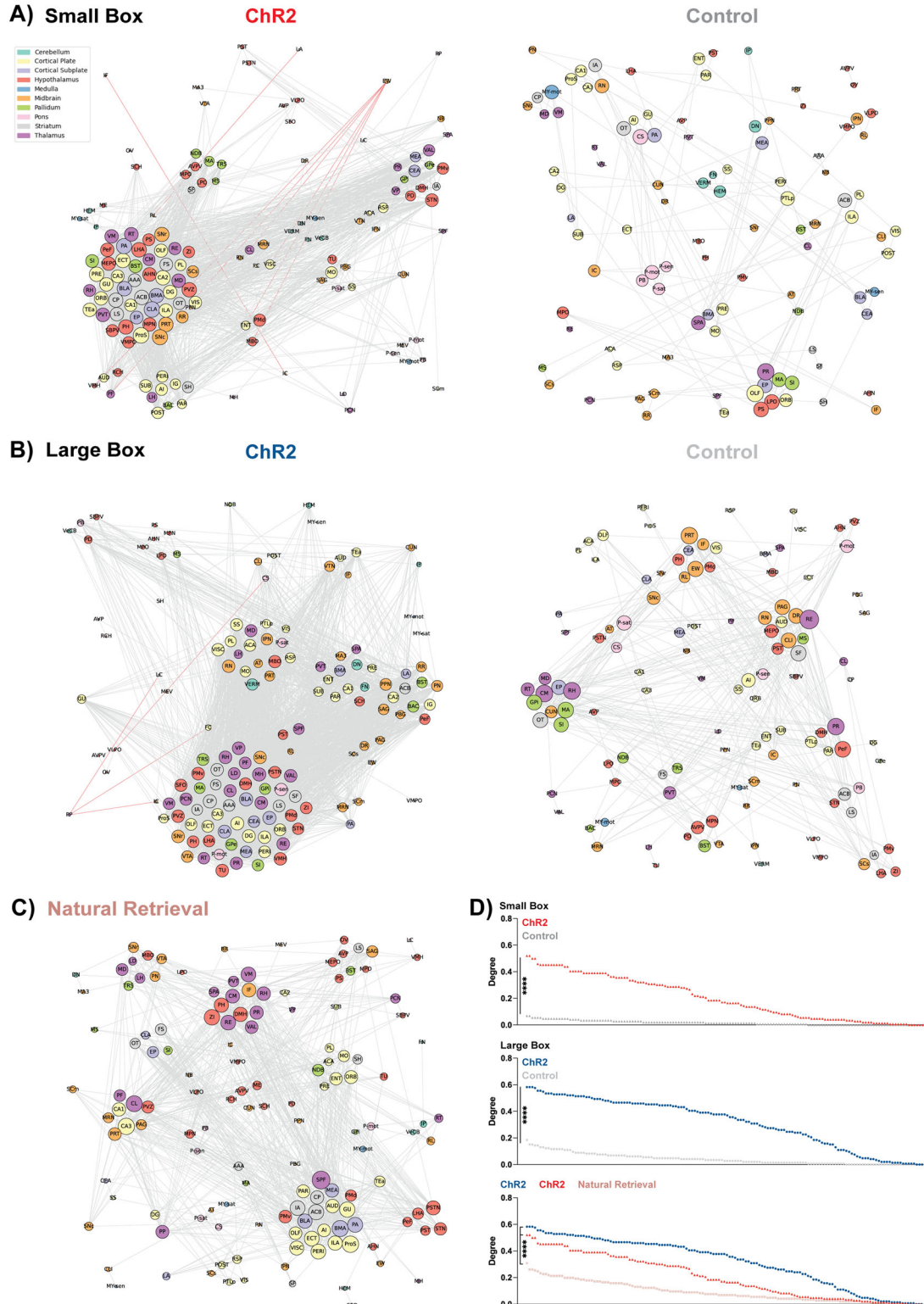


**Figure 9.** Engram reactivation creates unique network topologies. **A**, ChR2 (left) and control (right) networks generated in the SB condition. **B**, ChR2 (left) and control (right) networks generated in the LB condition. **C**, Natural retrieval network generated in the original fear conditioning context. **D**, Degree rank plot for all 147 nodes across all experimental conditions. There were significantly higher-degree nodes in ChR2 networks across both the SB (top) and LB (middle) environments when compared to controls. Additionally, both ChR2 groups had greater high-degree nodes than the natural retrieval group and the LB ChR2 had a significantly greater distribution of high-degree nodes than the ChR2 SB group (bottom). +Gray-colored edges are positive correlations whereas red edges are negative. Edges were only kept if the Spearman correlation coefficient survived a 5% FDR correction. ++Nodes are colored by their respective Figure 7F ‘Parent Region’ (Fig. 4A, legend). Communities are denoted by their spatial proximity, i.e., communities are clustered together in circular shapes within the networks. Communities were discovered using the Leiden algorithm.

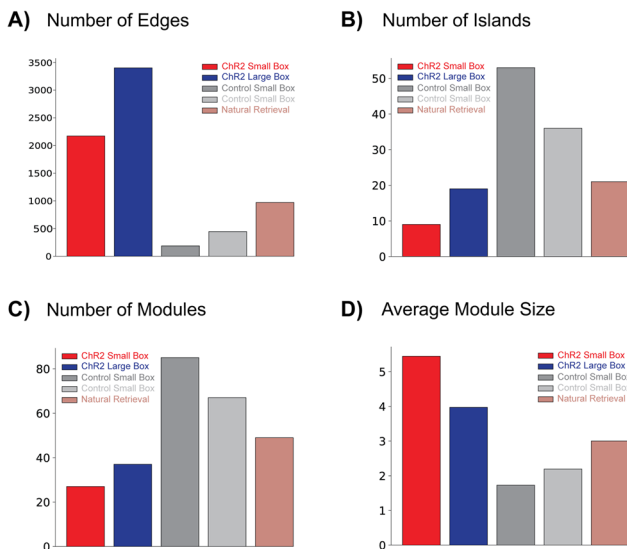


**Figure 10.** The network structure is not comparable across experimental conditions. **A**, The number of edges in each network. There are more significant edges left after the 5% FDR correction in both Chr2 networks relative to the Control and natural retrieval groups. **B**, The number of island nodes (i.e., nodes with zero connections) for each network. There are higher island nodes in the control networks relative to both Chr2 networks. **C**, # of modules as a result of applying the Leiden community detection algorithm for each network. There are more modules in both Control and natural retrieval networks than there are in both Chr2 networks. **D**, Average module size for each network. Although the Chr2 group had fewer modules, the average size of their respective modules was much greater than the average size of the modules in the control and natural retrieval groups.

manipulations. Collectively, these findings provide an extensive list of candidate central hubs that could be functionally perturbed *in vivo* and are differentially recruited across environments, furthering the evidence that these networks are distinct.

The application of clustering algorithms functionally segregates nodes based on shared correlation composition across the network. Thus, we further characterized nodes by how they communicated within and across clustered modules (Fig. 9). For each node, we generated a respective WMDz and PC (Guimerà and Nunes Amaral, 2005). Nodes that had a WMDz score of  $>1$  are considered highly important for intra-module signaling after the Leiden community detection algorithm was applied. A node having a PC  $> 0.5$  is important for inter-module connectivity. We defined modular hubs as having both a WMDz score of 1.0 or above and a PC score of 0.5 or higher (Fig. 12A,C,E). Interestingly, we found that there are no shared community-based hubs across Chr2 and control networks in the SB condition (Fig. 12B). However modular hubs in the Chr2 SB condition are regions that are implicated in memory or behavior (i.e., MS, ProS, CLA, MEA). Other modular hubs in the Chr2 LB condition are also implicated in memory or behavior (i.e., BLA, AI) (Fig. 12D). Interestingly, the CLA was a shared hub across groups in the LB condition, which could be attributed to its role in mediating anxiety responses (Niu et al., 2022). Finally, when we compared modular hubs across all Chr2 groups and natural retrieval, we were surprised to find no shared hubs across either Chr2 group with natural retrieval, yet the CLA was shared across both Chr2 groups (Fig. 12F). However, unique modular hubs in the natural retrieval group included regions heavily implicated in memory or defensive behavior (i.e., LHA, BST, BMA, ENT). These findings also suggest that hippocampal CFC engram reactivation produces a different brain state from natural retrieval even though freezing across the two groups was equivocal.

Overall, these results qualitatively show that there are unique patterns of coactivation as a result of DG-centered CFC engram reactivation.

## Discussion

Our results demonstrate that hippocampal CFC engram reactivation can drive freezing in a manner that is conditionally dependent on training and environmental context. Furthermore, artificial reactivation of hippocampal CFC engrams under different environments induced whole-brain cFos activity in a distinct manner between environments, and network hub regions mediating memory and behavior play a more active role in our experimental groups.

Our initial behavioral findings suggest that light-induced freezing becomes more apparent as the size of an environment becomes constrained; ChR2-injected mice conditioned in a small chamber demonstrated robust light-induced freezing in the SB condition, an intermediate amount of light-induced freezing in the MB, but no light-induced freezing in the LB. Previous studies examining innate fear responses during TMT exposure also show this relationship between the environment size and freezing (Wallace and Rosen, 2000; Rosen et al., 2008). Rodents exposed to TMT in smaller arenas often defaulted to freezing; others opted for more active ambulatory responses such as avoidance as environments were less spatially constrained. However, an additional interpretation is that our results are due to contextual congruence between the small CFC chamber and the SB during hippocampal CFC engram reactivation, as similar cues could trigger fear responses (Frankland et al., 2019; Jung et al., 2023). To test this idea, we created a larger CFC chamber to tag a hippocampal CFC engram to reactivate across the three environments. While there was a lack of light-induced freezing in the LB during hippocampal CFC engram reactivation, we did observe engram ensemble overlap with cFos. Thus, we obtained congruent representation at the level of cell populations without freezing emerging as the predominant behavioral phenotype. Taken together, this indicates that the congruence of both reactivation and initial training conditions are important variables in determining if engram reactivation is capable of inducing freezing behavior. This finding is incredibly important for interpreting prior and future engram literature as this means that behavioral responses to engram reactivation are flexible in nature.

Historically, bidirectional light-induced freezing was the standard for successful engram reactivation in CFC studies, but our results suggest this standard is incomplete; hippocampal CFC engrams are not guaranteed to solely produce freezing, and finding alternative behavioral or physiological measures will be necessary to study engrams across diverse experimental paradigms. In support, recent research suggests that activated fear engrams are sufficient to drive active avoidance-like behaviors in large arenas (Ramirez et al., 2013; Redondo et al., 2014; Chen et al., 2019). Although we did not observe any avoidance-like phenotypes and selective light-induced freezing, a negative affective state such as fear can manifest as a variety of behaviors across sexes (Blanchard and Blanchard, 1989; Colom-Lapetina et al., 2019). There are many defensive strategies that animals implement depending on their situation (Bolles, 1970; Fanselow and Lester, 1988; Grossen and Kelley, 1972; Blanchard and Blanchard, 2008). Defensive behaviors include, but are not limited to, tail rattling as a sign of defensive aggression (Salay et al., 2018), risk assessment via stretch-attend

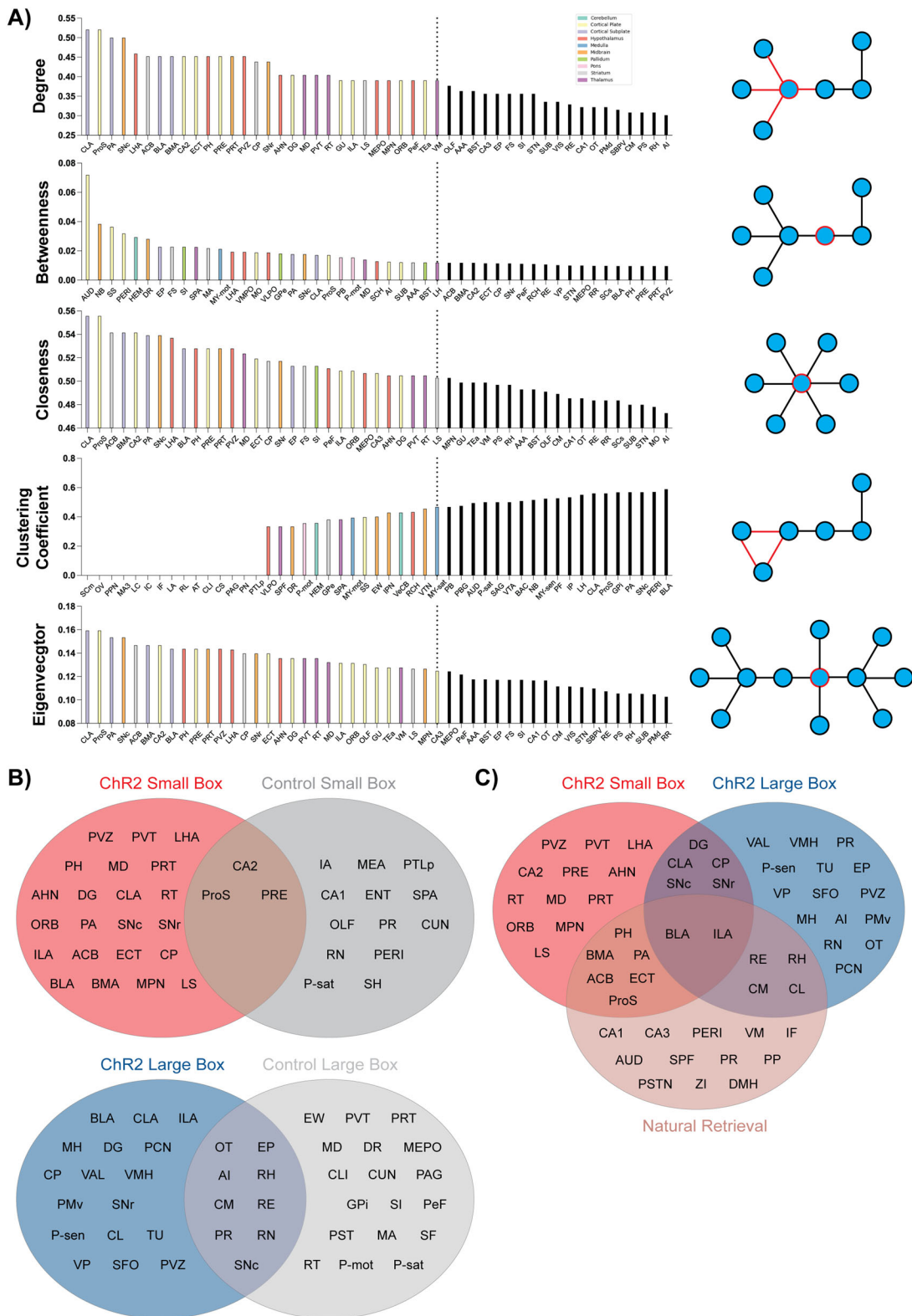


**Figure 11.** Regions involving memory and defensive behavior act as central hubs in ChR2 and natural retrieval networks. **A**, The distribution of 50 nodes along five centrality metrics (degree, betweenness, closeness, clustering coefficient, and eigenvector) for the ChR2 SB network. “Hub scores” were generated for all 147 nodes in the network. Nodes falling into the top 20% (degree, betweenness, closeness, eigenvector) or bottom 20% (clustering coefficient) received a + 1. Nodes that fell in these distributions were assigned colors based on their anatomical location. **B**, Central hubs for both ChR2 and control groups in the SB and LB conditions. We define central hubs as having a score of three or greater. Shared hubs lie in the intersection of the two groups. **C**, Central hubs for both ChR2 groups and the natural retrieval condition. We define central hubs as having a score of three or greater. Shared hubs lie in the intersection of the two groups.

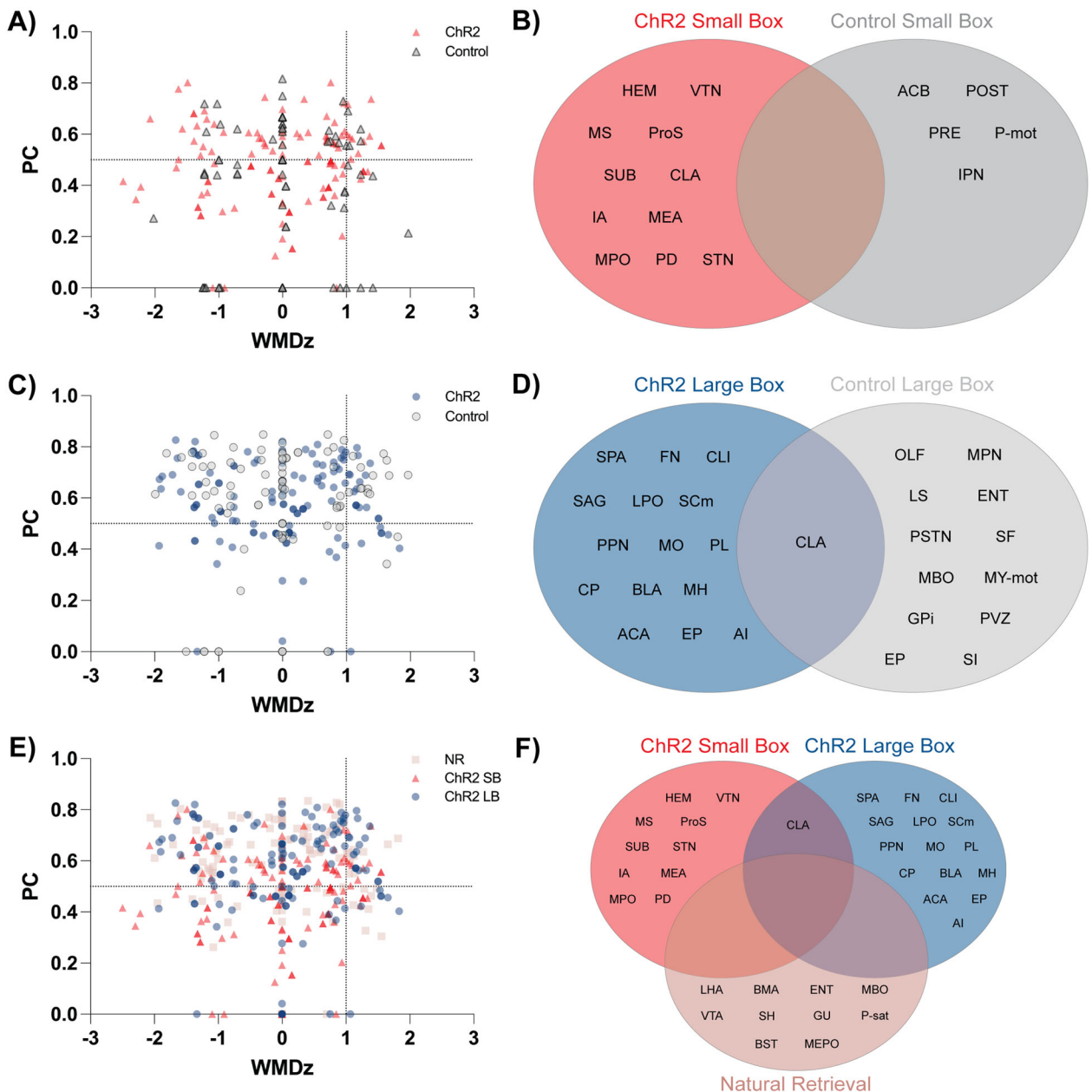


**Figure 12.** Regions involving memory and behavior act as modular hubs in ChR2 conditions and natural retrieval conditions. **A**, WMDz and participation coefficient (PC) were generated for all 147 regions for the ChR2 and control groups in the SB environment. Classification of a modular hub would pass a WMDz threshold of 1.0 and a PC threshold of 0.5. **B**, There were no shared modular hubs across groups in the SB condition. Yet, regions implicated in memory and behavior still serve as unique modular hubs in the ChR2 group. **C**, WMDz and PC were generated for all 147 regions for the ChR2 and control groups in the LB environment. Classification of a modular hub would pass a WMDz threshold of 1.0 and a PC threshold of 0.5. **D**, The CLA was the only shared hub across the ChR2 and Control groups in the LB. The ChR2 group also contained unique modular hubs implicated in memory and behavior. **E**, WMDz and PC were generated for all 147 regions for the ChR2 groups and the natural retrieval group. Classification of a modular hub would pass a WMDz threshold of 1.0 and a PC threshold of 0.5. **F**, The CLA was the only shared modular hub region between both ChR2 groups, yet there were also no shared modular hubs with the natural retrieval group. Unique modular hubs in the natural retrieval condition are also implicated in memory and defensive behavior.

posture (Molewijk et al., 1995), rearing as a form of escape-seeking (Lever et al., 2006), jumping as a means of escape (Mangieri et al., 2019), and self-grooming as a de-arousal technique after an aversive experience (Kalueff et al., 2016; Song et al., 2016; Liu et al., 2021). Other defensive behaviors such as darting are sex-dependent in dimorphic species such as rodents (Gruene et al., 2015; Shansky and Murphy, 2021). Thus, we speculate that animals may engage in a variety of these behavioral modalities during hippocampal CFC engram reactivation under different environmental conditions, which may also be sex-dependent in nature. Advanced methods in behavioral analysis

such as DeepLabCut, MoSeq, and BehaviorDEPOT could decipher high-resolution behavioral repertoires during hippocampal CFC engram reactivation across environments (Mathis et al., 2018; Wiltschko et al., 2020; Gabriel et al., 2022). Future studies can also examine the behavioral effects of hippocampal CFC engram reactivation while incorporating more complex environments such as one containing an exit or shelter that warrants the rodent to engage in more navigation-based escape strategies (Vale et al., 2017; Salay et al., 2018; Mangieri et al., 2019; Wang et al., 2021). We predict that the latency for seeking either an exit or shelter would decrease at the onset of hippocampal CFC

engram reactivation, which may also be subsequently accompanied by light-induced freezing or other defensive behaviors such as stretch–attend posture. This collectively underscores the behavioral flexibility driven by activated DG engram cells. Indeed, there are a variety of interleaving brain-wide pathways that mediate these alterations in defensive behavioral strategies (Fanselow, 1994; Fendt and Fanselow, 1999; Gross and Canteras, 2012; Silva et al., 2016), which points to the capacity for hippocampal CFC engrams to produce changes in internal brain states.

Our brain-wide analyses revealed that optical stimulation of a hippocampal CFC engram is capable of globally increasing cFos expression. This dovetails with recent work showing that CA1 engram ensemble reactivation functionally recruits regions downstream in a brain-wide manner as indicated by increased cFos (Roy et al., 2022). We also found increased cFos expression in both of our ChR2 groups in comparison to their respective Control groups, despite that freezing was only present in the SB condition, which underscores the complexity of behavioral and physiological correlates of hippocampal CFC engram reactivation. Furthermore, these changes in cFos density in both ChR2 groups coincide with greater positive Spearman correlations, indicating that our optical stimulation is coordinating the brain's activity at the network level. This level of coactivation is not seen in either Control group, which suggests that artificial memory activation pushes global brain activity to a state of greater functional connectivity. These data are further complimented by our UMAP results, which show that brain regions are segregated not by their parental region (e.g., cortical subplate, hypothalamus) but rather by their experimental condition, suggesting that each condition elicited a unique pattern of brain activity. Future experiments could identify how the reactivation of a homecage or “neutral” context engram is capable of changing brain-wide activity. We hypothesize that neutral engram reactivation would increase global cFos as a result of direct hippocampus stimulation but would still show a unique pattern of activity in comparison to the Control or CFC engram groups, as each brain region pattern of correlation coefficients is a multivariate distribution. Thus, since UMAP, in theory, will segregate regions based on both the magnitudes and the patterns of activation, merely increasing correlated activity across the brain would not necessarily elicit similar patterns of correlation in a neutral or homecage engram reactivation group.

Through our community detection analyses, we probed which regions of the brain were more densely connected to one another. The ChR2 groups displayed qualitatively similar modular structures in that they had fewer but denser communities than their respective Control groups. It is possible that our engram manipulations are creating negative affective states with unique corresponding brain states across our environmental conditions. For example, the light-induced freezing in the SB generated a network that clustered hypothalamic, thalamic, amygdalar, and hippocampal regions that span a “fear pathway” (Fanselow, 1994; Fendt and Fanselow, 1999; Gross and Canteras, 2012; Silva et al., 2016) and exhibited more edge connections than the respective control network, whose animals did not exhibit any fear-like behavior. Modules in both ChR2 networks were also more heterogeneous in node composition compared to the natural retrieval network. The natural retrieval network had modules that contained mostly hippocampal or thalamic regions and some that were solely hypothalamic regions. This heterogeneity in our ChR2 networks may indicate that our stimulation increases correlated activity across neural circuitry that causes heightened fear responses, even if not behaviorally observable or measured here (i.e., lack of light-induced

freezing in the LB). Interestingly, naturalistic and light-induced freezing across the natural retrieval and ChR2 SB conditions were not significantly different, which could be partly explained by a phenomenon known as biological degeneracy, where two different physiological states can cause the same behavior (Edelman and Gally, 2001; Marder and Taylor, 2011). Previous works demonstrated degenerative networks across rodent strains (Wheeler et al., 2013), timescales (Wheeler et al., 2013), and biological sex (du Pleiss et al., 2022) to produce similar behavioral outcomes across groups during either fear memory retrieval or conditioning.

In network science, hubs are nodes that are crucial for mediating signal propagation throughout the network. Here, we quantified a series of centrality metrics and examined the distribution of all 147 nodes across these metrics to identify central hubs (van den Heuvel et al., 2010; van den Heuvel and Sporns, 2013) and found many unique and shared central hubs across experimental conditions. In the SB ChR2 and control networks, the only shared central hubs were CA2, the prosubiculum (ProS), and the presubiculum (PRE)—all of which are involved in hippocampal-mediated memory systems (Aggleton and Christiansen, 2015; Roy et al., 2017; Lehr et al., 2021). Conversely, the LB experimental and control networks shared many hubs implicated in locomotion, such as the red nucleus (RN; Basile et al., 2021), substantia nigra pars compacta (SNC; Palmiter, 2008), and regions that interface with cortical and hippocampal areas such as the reunions (RE) and rhomboid nucleus (RH), both of which have direct reciprocal anatomical connections (Cassel et al., 2013). This implies that both sets of animals could be in a general anxiogenic state due to being exposed in a spatially large arena with no coverage indicative of safety. Predictably, we found the DG and BLA as unique central hubs in the ChR2 LB, as we reactivated the tagged hippocampal CFC engram, and previous work has shown functional recruitment of the BLA after hippocampal CFC engram reactivation (Ramirez et al., 2013; Redondo et al., 2014; Ryan et al., 2015). Of note are the shared central hubs between both ChR2 and natural retrieval networks. All three networks shared the BLA and the ILA, both of which are highly implicated in producing fear responses (Fanselow, 1994; Fendt and Fanselow, 1999; Dalley et al., 2004; Herry and Johansen, 2014; Powell and Redish, 2016). These findings generate an extensive list of candidate hub regions for future perturbation experiments to test for hub region necessity in generating light-induced behavioral phenotypes during hippocampal CFC engram reactivation (Vetere et al., 2017). Surprisingly, the DG is only present in the ChR2 networks, but not in natural retrieval. Our findings suggest that although the DG has been shown to be necessary and sufficient for memory retrieval (McHugh et al., 2007; Liu et al., 2012), in the natural expression of fear, it is not the seat of memory per se but a part of a much larger connected network (Hainmueller and Bartos, 2020). Furthermore, in the natural retrieval group CA1 and CA3 were found to be hubs, but not in the ChR2 groups. This is an intriguing result as the hippocampus contains well-characterized connections, yet contemporary work suggests that information propagation within the hippocampus is not solely serial through these connections but in multiple parallel streams (Hainmueller and Bartos, 2020). The artificial nature of optogenetic stimulation may be increasing recruitment of hub regions spanning “fear and defense” pathways (i.e., thalamic, hypothalamic, and midbrain areas) than naturalistic retrieval alone. However, it is worth noting that “hub” can be a loosely defined term, and the work presented here puts forth one possible definition. Other algorithms have been proposed that leverage

the Laplacian matrix of a network (Hong et al., 2021), graph embeddings (Ma et al., 2017), or persistent homology (Aktas et al., 2019) to detect hubs. Future work could lead to further interpretations of biologically informed networks. Taken together, our work bridges both biological- and network-based approaches for studying memory and behavior.

## Data availability statement

All code is freely available in the following GitHub repository: [https://github.com/rsenne/network\\_analysis](https://github.com/rsenne/network_analysis). All data will be made available upon reasonable request.

## References

- Aggleton JP, Christiansen K (2015) Chapter 4: The subiculum: the heart of the extended hippocampal system. In: *Progress in brain research* (O'Mara S Tsanov M, ed), pp 65–82; Elsevier. The connected hippocampus.
- Aktas ME, Akbas E, Fatmaoui AE (2019) Persistence homology of networks: methods and applications. *Appl Netw Sci* 4:1–28.
- Amano T, Duvarci S, Popa D, Pare D (2011) The fear circuit revisited: contributions of the basal amygdala nuclei to conditioned fear. *J Neurosci* 31:15481–15489.
- Basile GA, Quartu M, Bertino S, Serra MP, Boi M, Bramanti A, Anastasi GP, Milardi D, Cacciola A (2021) Red nucleus structure and function: from anatomy to clinical neurosciences. *Brain Struct Funct* 226:69–91.
- Benjamini Y, Hochberg Y (1995) Controlling the false discovery rate: a practical and powerful approach to multiple testing. *J R Stat Soc Ser B Methodol* 57:289–300.
- Berg S, et al. (2019) ilastik: interactive machine learning for (bio)image analysis. *Nat Methods* 16:1226–1232.
- Blanchard DC, Blanchard RJ (2008) Chapter 2.4 Defensive behaviors, fear, and anxiety. In: *Handbook of behavioral neuroscience*, pp 63–79; Elsevier.
- Blanchard RJ, Blanchard DC (1989) Attack and defense in rodents as ethoexperimental models for the study of emotion. *Prog Neuropsychopharmacol Biol Psychiatry* 13:S3–S14.
- Blondel VD, Guillaume J-L, Lambiotte R, Lefebvre E (2008) Fast unfolding of communities in large networks. *J Stat Mech Theory Exp* 2008:P10008.
- Bolles RC (1970) Species-specific defense reactions and avoidance learning. *Psychological Review* 77: 32–48.
- Cassel J-C, de Vasconcelos AP, Loureiro M, Cholvin T, Dalrymple-Alford JC, Vertes RP (2013) The reunions and rhomboid nuclei: neuroanatomy, electrophysiological characteristics and behavioral implications. *Prog Neurobiol* 111:34–52.
- Chen BK, et al. (2019) Artificially enhancing and suppressing hippocampus-mediated memories. *Curr Biol* 29:1885–1894.e4.
- Coelho CAO, Ferreira TL, Kramer-Soares JC, Sato JR, Oliveira MGM (2018) Network supporting contextual fear learning after dorsal hippocampal damage has increased dependence on retrosplenial cortex Bush D, ed. *PLOS Comput Biol* 14:e1006207.
- Colom-Lapetina J, Li AJ, Pelegrina-Perez TC, Shansky RM (2019) Behavioral diversity across classic rodent models is sex-dependent. *Front Behav Neurosci* 13:45.
- Cursio (2001) Genetic dissection of mouse exploratory behaviour. Available at: .
- Dalley JW, Cardinal RN, Robbins TW (2004) Prefrontal executive and cognitive functions in rodents: neural and neurochemical substrates. *Neurosci Biobehav Rev* 28:771–784.
- Dean KM, Roudot P, Welf ES, Danuser G, Fiolka R (2015) Deconvolution-free subcellular imaging with axially swept light sheet microscopy. *Biophys J* 108:2807–2815.
- Deng H, Xiao X, Wang Z (2016) Periaqueductal gray neuronal activities underlie different aspects of defensive behaviors. *J Neurosci* 36:7580–7588.
- Do-Monte FH, Quiñones-Laracuente K, Quirk GJ (2015) A temporal shift in the circuits mediating retrieval of fear memory. *Nature* 519:460–463.
- du Plessis KC, Basu S, Rumbell TH, Lucas EK (2022) Sex-specific neural networks of cued threat conditioning: a pilot study. *Front Syst Neurosci* 16: 832484.
- Edelman GM, Gally JA (2001) Degeneracy and complexity in biological systems. *Proc Natl Acad Sci* 98:13763–13768.
- Fadok JP, et al. (2017) A competitive inhibitory circuit for selection of active and passive fear responses. *Nature* 542:96–100.
- Fanselow MS (1994) Neural organization of the defensive behavior system responsible for fear. *Psychon Bull Rev* 1:429–438.
- Fanselow MS, Dong H-W (2010) Are the dorsal and ventral hippocampus functionally distinct structures? *Neuron* 65:7–19.
- Fanselow MS, Lester LS (1988) A functional behavioristic approach to aversively motivated behavior: predatory imminence as a determinant of the topography of defensive behavior. In: *Evolution and learning*, pp 185–212. Hillsdale, NJ, US: Lawrence Erlbaum Associates, Inc.
- Fendt M, Fanselow MS (1999) The neuroanatomical and neurochemical basis of conditioned fear. *Neurosci Biobehav Rev* 23:743–760.
- Fortunato S, Newman MEJ (2022) 20 years of network community detection. *Nat Phys* 18:848–850.
- Frankland PW, Josselyn SA, Köhler S (2019) The neurobiological foundation of memory retrieval. *Nat Neurosci* 22:1576–1585.
- Gabriel CJ, et al. (2022) BehaviorDEPOT is a simple, flexible tool for automated behavioral detection based on markerless pose tracking. Berman GJ, Colgin LL, eds. *Elife* 11:e74314.
- Glickman ME, Rao SR, Schultz MR (2014) False discovery rate control is a recommended alternative to Bonferroni-type adjustments in health studies. *J Clin Epidemiol* 67:850–857.
- Griebel G, Blanchard DC, Blanchard RJ (1996) Evidence that the behaviors in the mouse defense test battery relate to different emotional states: a factor analytic study. *Physiol Behav* 60:1255–1260.
- Gross CT, Canteras NS (2012) The many paths to fear. *Nat Rev Neurosci* 13: 651–658.
- Grossen NE, Kelley MJ (1972) Species-specific behavior and acquisition of avoidance behavior in rats. *J Comp Physiol Psychol* 81:307–310.
- Gruene TM, Flick K, Stefano A, Shea SD, Shansky RM (2015) Sexually divergent expression of active and passive conditioned fear responses in rats. *Elife* 4:e11352.
- Guimerà R, Nunes Amaral LA (2005) Functional cartography of complex metabolic networks. *Nature* 433:895–900.
- Hainmueller T, Bartos M (2020) Dentate gyrus circuits for encoding, retrieval and discrimination of episodic memories. *Nat Rev Neurosci* 21:153–168.
- He K, Zhang X, Ren S, Sun J (2015) Deep residual learning for image recognition. Available at: <https://arxiv.org/abs/1512.03385v1>.
- Henry C, Johansen JP (2014) Encoding of fear learning and memory in distributed neuronal circuits. *Nat Neurosci* 17:1644–1654.
- Hong Y, Chang I, Kim C (2021) Detection of hubs in complex networks by the Laplacian matrix. *J Korean Stat Soc* 50:431–446.
- Jardim MC, Guimarães FS (2004) Role of glutamate ionotropic receptors in the dorsomedial hypothalamic nucleus on anxiety and locomotor behavior. *Pharmacol Biochem Behav* 79:541–546.
- Jimenez JC, et al. (2018) Anxiety cells in a hippocampal-hypothalamic circuit. *Neuron* 97:670–683.e6.
- Josselyn SA, Tonegawa S (2020) Memory engrams: recalling the past and imagining the future. *Science* 367:eaaw4325.
- Jung JH, Wang Y, Mocle AJ, Zhang T, Köhler S, Frankland PW, Josselyn SA (2023) Examining the engram encoding specificity hypothesis in mice. *Neuron* 111:1830–1845.
- Kalueff AV, Stewart AM, Song C, Berridge KC, Graybiel AM, Fentress JC (2016) Neurobiology of rodent self-grooming and its value for translational neuroscience. *Nat Rev Neurosci* 17:45–59.
- Keller D, Erö C, Markram H (2018) Cell densities in the mouse brain: a systematic review. *Front Neuroanat* 12:83.
- Kim JJ, Rison RA, Fanselow MS (1993) Effects of amygdala, hippocampus, and periaqueductal gray lesions on short- and long-term contextual fear. *Behav Neurosci* 107:1093–1098.
- Kim S-Y, et al. (2013) Diverging neural pathways assemble a behavioural state from separable features in anxiety. *Nature* 496:219–223.
- Kim S-Y, et al. (2015) Stochastic electrotransport selectively enhances the transport of highly electromobile molecules. *Proc Natl Acad Sci* 112:E6274–83.
- Lehr AB, Kumar A, Tetzlaff C, Hafting T, Fyhn M, Stöber TM (2021) CA2 beyond social memory: evidence for a fundamental role in hippocampal information processing. *Neurosci Biobehav Rev* 126:398–412.
- Lever C, Burton S, O'Keefe J (2006) Rearing on hind legs, environmental novelty, and the hippocampal formation. *Rev Neurosci* 17:111–33.
- Lin D, Boyle MP, Dollar P, Lee H, Lein ES, Perona P, Anderson DJ (2011) Functional identification of an aggression locus in the mouse hypothalamus. *Nature* 470:221–226.
- Liu H, et al. (2021) Dissection of the relationship between anxiety and stereotyped self-grooming using the Shank3B mutant autistic model, acute stress model and chronic pain model. *Neurobiol Stress* 15:100417.

- Liu X, Ramirez S, Pang PT, Puryear CB, Govindarajan A, Deisseroth K, Tonegawa S (2012) Optogenetic stimulation of a hippocampal engram activates fear memory recall. *Nature* 484:381–385.
- Ma G, Lu C-T, He L, Yu PS, Ragin AB (2017) Multi-view graph embedding with hub detection for brain network analysis. Available at: .
- Ma J, du Hoffmann J, Kindel M, Beas BS, Chudasama Y, Penzo MA (2021) Divergent projections of the paraventricular nucleus of the thalamus mediate the selection of passive and active defensive behaviors. *Nat Neurosci* 24:1429–1440.
- Mangieri LR, Jiang Z, Lu Y, Xu Y, Cassidy RM, Justice N, Xu Y, Arenkiel BR, Tong Q (2019) Defensive behaviors driven by a hypothalamic-ventral midbrain circuit. *eNeuro* 6:1–19.
- Marder E, Taylor AL (2011) Multiple models to capture the variability in biological neurons and networks. *Nat Neurosci* 14:133–138.
- Maren S, Phan KL, Liberzon I (2013) The contextual brain: implications for fear conditioning, extinction and psychopathology. *Nat Rev Neurosci* 14: 417–428.
- Mathis A, Mamidanna P, Cury KM, Abe T, Murthy VN, Mathis MW, Bethge M (2018) DeepLabCut: markerless pose estimation of user-defined body parts with deep learning. *Nat Neurosci* 21:1281–1289.
- McHugh TJ, Jones MW, Quinn JJ, Balthasar N, Coppari R, Elmquist JK, Lowell BB, Fanselow MS, Wilson MA, Tonegawa S (2007) Dentate gyrus NMDA receptors mediate rapid pattern separation in the hippocampal network. *Science* 317:94–99.
- McInnes L, Healy J, Melville J (2020) UMAP: uniform manifold approximation and projection for dimension reduction. Available at: .
- Meyer MAA, Corcoran KA, Chen HJ, Gallego S, Li G, Tiruveedhula VV, Cook JM, Radulovic J (2017) Neurobiological correlates of state-dependent context fear. *Learn Mem* 24:385–391.
- Milad MR, Quirk GJ (2012) Fear extinction as a model for translational neuroscience: ten years of progress. *Annu Rev Psychol* 63:129–151.
- Molewijk HE (1995) The ambivalent behaviour “stretched approach posture” in the rat as a paradigm to characterize anxiolytic drugs.
- Mu M-D, Geng H-Y, Rong K-L, Peng R-C, Wang S-T, Geng L-T, Qian Z-M, Yung W-H, Ke Y (2020) A limbic circuitry involved in emotional stress-induced grooming. *Nat Commun* 11:2261.
- Niu M, et al. (2022) Claustrum mediates bidirectional and reversible control of stress-induced anxiety responses. *Sci Adv* 8:eabi6375.
- Oh SW, et al. (2014) A mesoscale connectome of the mouse brain. *Nature* 508: 207–214.
- Palmiter RD (2008) Dopamine signaling in the dorsal striatum is essential for motivated behaviors: lessons from dopamine-deficient mice. *Ann N Y Acad Sci* 1129:35–46.
- Park Y-G, et al. (2019) Protection of tissue physicochemical properties using polyfunctional crosslinkers. *Nat Biotechnol* 37:73–83.
- Penzo MA, et al. (2015) The paraventricular thalamus controls a central amygdala fear circuit. *Nature* 519:455–459.
- Pobbe RLH, Zangrossi H (2010) The lateral habenula regulates defensive behaviors through changes in 5-HT-mediated neurotransmission in the dorsal periaqueductal gray matter. *Neurosci Lett* 479:87–91.
- Powell NJ, Redish AD (2016) Representational changes of latent strategies in rat medial prefrontal cortex precede changes in behaviour. *Nat Commun* 7:12830.
- Ramirez S, Liu X, Lin P-A, Suh J, Pignatelli M, Redondo RL, Ryan TJ, Tonegawa S (2013) Creating a false memory in the hippocampus. *Science* 341:387–391.
- Ramirez S, Liu X, MacDonald CJ, Moffa A, Zhou J, Redondo RL, Tonegawa S (2015) Activating positive memory engrams suppresses depression-like behaviour. *Nature* 522:335–339.
- Redondo RL, Kim J, Arons AL, Ramirez S, Liu X, Tonegawa S (2014) Bidirectional switch of the valence associated with a hippocampal contextual memory engram. *Nature* 513:426–430.
- Reijmers LG, Perkins BL, Matsuo N, Mayford M (2007) Localization of a stable neural correlate of associative memory. *Science* 317:1230–1233.
- Ronneberger O, Fischer P, Brox T (2015) U-Net: Convolutional networks for biomedical image segmentation. *ArXiv*: 1–8. Available at: <https://arxiv.org/abs/1505.04597v1>.
- Rosen JB, Pagani JH, Rolla KLG, Davis C (2008) Analysis of behavioral constraints and the neuroanatomy of fear to the predator odor trimethylthiazoline: a model for animal phobias. *Neurosci Biobehav Rev* 32:1267–1276.
- Roy DS, Arons A, Mitchell TI, Pignatelli M, Ryan TJ, Tonegawa S (2016) Memory retrieval by activating engram cells in mouse models of early Alzheimer’s disease. *Nature* 531:508–512.
- Roy DS, Kitamura T, Okuyama T, Ogawa SK, Sun C, Obata Y, Yoshiki A, Tonegawa S (2017) Distinct neural circuits for the formation and retrieval of episodic memories. *Cell* 170:1000–1012.e19.
- Roy DS, et al. (2022) Brain-wide mapping reveals that engrams for a single memory are distributed across multiple brain regions. *Nat Commun* 13:1799.
- Ryan TJ, Roy DS, Pignatelli M, Arons A, Tonegawa S (2015) Engram cells retain memory under retrograde amnesia. *Science* 348:1007–1013.
- Salay LD, Ishiko N, Huberman AD (2018) A midline thalamic circuit determines reactions to visual threat. *Nature* 557:183–189.
- Scoville WB, Milner B (1957) Loss of recent memory after bilateral hippocampal lesions. *J Neurol Neurosurg Psychiatry*. 20:11–21.
- Shansky RM, Murphy AZ (2021) Considering sex as a biological variable will require a global shift in science culture. *Nat Neurosci* 24:457–464.
- Shelhamer E, Long J, Darrell T (2016) Fully convolutional networks for semantic segmentation. Available at: <https://arxiv.org/abs/1605.06211v1>.
- Sierra-Mercado D, Padilla-Coreano N, Quirk GJ (2011) Dissociable roles of prelimbic and infralimbic cortices, ventral hippocampus, and basolateral amygdala in the expression and extinction of conditioned fear. *Neuropsychopharmacology* 36:529–538.
- Silva BA, Burns AM, Gräff J (2019) A cFos activation map of remote fear memory attenuation. *Psychopharmacology* 236:369–381.
- Silva BA, Gross CT, Gräff J (2016) The neural circuits of innate fear: detection, integration, action, and memorization. *Learn Mem* 23:544–555.
- Song C, Berridge KC, Kaluza AV (2016) “Stressing” rodent self-grooming for neuroscience research. *Nat Rev Neurosci* 17:591–591.
- Soria-Gómez E, et al. (2015) Habenular CB1 receptors control the expression of aversive memories. *Neuron* 88:306–313.
- Stamatakis AM, Stuber GD (2012) Activation of lateral habenula inputs to the ventral midbrain promotes behavioral avoidance. *Nat Neurosci* 15: 1105–1107.
- Swaney J, Kamensky L, Evans NB, Xie K, Park Y-G, Drummond G, Yun DH, Chung K (2019) Scalable image processing techniques for quantitative analysis of volumetric biological images from light-sheet microscopy. *BioRxiv*:1–32.
- Terstege DJ, Epp JR (2022) Network neuroscience untethered: brain-wide immediate early gene expression for the analysis of functional connectivity in freely behaving animals. *Biology* 12:34.
- Tovote P, Fadok JP, Lüthi A (2015) Neuronal circuits for fear and anxiety. *Nat Rev Neurosci* 16:317–331.
- Tovote P, et al. (2016) Midbrain circuits for defensive behaviour. *Nature* 534: 206–212.
- Traag VA, Waltman L, van Eck NJ (2019) From Louvain to Leiden: guaranteeing well-connected communities. *Sci Rep* 9:5233.
- Vale R, Evans DA, Branco T (2017) Rapid spatial learning controls instinctive defensive behavior in mice. *Curr Biol* 27:1342–1349.
- van den Heuvel MP, Mandl RCW, Stam CJ, Kahn RS, Hulshoff Pol HE (2010) Aberrant frontal and temporal complex network structure in schizophrenia: a graph theoretical analysis. *J Neurosci* 30:15915–15926.
- van den Heuvel MP, Sporns O (2013) Network hubs in the human brain. *Trends Cogn Sci* 17:683–696.
- Vetere G, Kenney JW, Tran LM, Xia F, Steadman PE, Parkinson J, Josselyn SA, Frankland PW (2017) Chemogenetic interrogation of a brain-wide fear memory network in mice. *Neuron* 94:363–374.e4.
- Wallace KJ, Rosen JB (2000) Predator odor as an unconditioned fear stimulus in rats: elicitation of freezing by trimethylthiazoline, a component of fox feces. *Behav Neurosci* 114:912–922.
- Wang W, et al. (2021) Coordination of escape and spatial navigation circuits orchestrates versatile flight from threats. *Neuron* 109:1848–1860.e8.
- Wheeler AL, Teixeira CM, Wang AH, Xiong X, Kovacevic N, Lerch JP, McIntosh AR, Parkinson J, Frankland PW (2013) Identification of a functional connectome for long-term fear memory in mice Sporns O, ed. *PLoS Comput Biol* 9:e1002853.
- Wiltschko AB, Tsukahara T, Zeine A, Anyoha R, Gillis WF, Markowitz JE, Peterson RE, Katon J, Johnson MJ, Datta SR (2020) Revealing the structure of pharmacobehavioral space through motion sequencing. *Nat Neurosci* 23:1433–1443.
- Yu K, Garcia da Silva P, Albeau DF, Li B (2016) Central amygdala somatosatin neurons gate passive and active defensive behaviors. *J Neurosci* 36: 6488–6496.
- Yun DH, et al. (2019) Ultrafast immunostaining of organ-scale tissues for scalable proteomic phenotyping. *BioRxiv*:1–28.
- Zhang J, et al. (2016) Presynaptic excitation via GABA B receptors in habenula cholinergic neurons regulates fear memory expression. *Cell* 166:716–728.